Controlled Organization of Silica Nanospheres into Highly Ordered Monolayers on a Substrate

Submitted to the
Faculty of Mathematics and Natural Sciences at
Heinrich-Heine-University Düsseldorf
in fulfillment to the requirement for B.Sc. degree in
Physics

Nadine Seidel
Mat.-No.:2425256

29.04.2024

First advisor: PD Dr. O. Petracic
Second advisor: Univ.-Prof. Dr. M. Getzlaff

Declaration of Authorship

I hereby declare, that I have written this bachelor thesis *"Controlled Organization of Silica Nanospheres into Highly Ordered Monolayers on a Substrate"* without any help from others and without the use of documents other than those specified. Besides, all utilized sources were provided in the reference list.

Eidesstaatliche Erklärung

Ich, Nadine Seidel, erkläre hiermit, dass ich diese Bachelorarbeit *"Controlled Organization of Silica Nanospheres into Highly Ordered Monolayers on a Substrate"* selbstständig und ohne Benutzung anderer als der angegebenen Quellen und Hilfsmittel verfasst habe. Alle wörtlich oder sinngemäß benutzten Quellen sind als solche einzeln kenntlich gemacht.

Place, Date	Nadine Seidel

Contents

Chapter 1

Introduction

The study of nanoparticle self-assembly has been of interest in the field of nanotechnology due to their broad range of potential applications. It allows for the creation of new nanomaterials with unique properties that differ from bulk materials. The distinctive properties of nanoparticles, such as their high surface area relative to their volume and enhanced quantum effects, facilitate the development of new technology across various industries. However, nanoparticles must be organized into ordered structures to be able to exhibit their characteristics in practical applications. Therefore, producing structures with long-range ordering is needed to utilize the functional properties of nanoparticles. To achieve this, nanoparticle self-assembly is a way to arrange nanoparticles into defined structures using interparticle and particle-substrate interactions.

In this thesis, the self-assembly of silica (SiO_2) nanoparticles with a diameter of 200 nm into ordered monolayers on a silicon substrate is investigated. Silica nanoparticles in particular offer great tunability of their physical, chemical, and optical properties, in addition to their low toxicity and good biocompatibility. They can be derived from biomass, making them not only cost-effective but also environmentally friendly. Fabricating monolayers from silica nanoparticles allows them to serve as a modulating substrate for the subsequent deposition of thin films, thereby enabling the tuning of properties such as optical, mechanical, and magnetic characteristics. For this, an improved version of drop-casting is used to fabricate the monolayers that includes the addition of stearyl alcohol to the nanoparticle dispersion. Then, a drop volume series investigation is conducted to determine the ideal drop volume as it is a key factor in the self-assembly process. This is fol-

lowed by an additional heat treatment step to improve the monolayer quality. The structural characterization of the SiO_2 was done by Scanning Electron Microscopy (SEM) to obtain local information, and by X-ray Reflectivity (XRR) and Grazing-Incidence Small-angle X-ray Scattering (GISAXS) for global average information.

Chapter 2

Theoretical Background

This chapter introduces the theoretical background of nanoparticle self-assembly and the techniques used to perform structural characterization. First, the current methods to achieve ordered structures using self-assembly and their basic principles behind particle interactions will be explained. Afterwards, the main theory behind the characterization methods is introduced.

2.1 Nanoparticle Self-Assembly

Self-assembly is a process where components of a system assemble into ordered structures without external guidance, irrespective of component size [1]. Self-assembly is not only observed in nature but also in artificial systems and can be influenced by controlling several factors. For example choosing materials as components that exhibit desired intermolecular forces (i.e. hydrogen bonds, Van-der-Waals forces), tuning their surface properties and regulating environmental conditions. In nature, processes that rely on self-assembly can be observed at various scales, from the molecular to the cosmic scale. For instance, biomolecular processes such as the assembly of nucleic acids into the double helix structure of DNA and RNA, or the formation of stars and planets from cosmic dust through gravitational forces into ordered structures that form galaxies illustrate the prevalence of self-assembly in nature.
In the context of nanostructures, nanoparticles can be used as building blocks to fabricate two- and three-dimensional structures, thereby enabling the creation of novel nanomaterials. The potential applications of self-assembled

nanomaterials encompass a diverse range of fields, from optical devices, such as ordered arrays in photonic crystals for optical devices [2], to electronic devices using ordered bimolecular-layered organic semiconductors [3, 4], and for enhancing the durability of Platinum (Pt) catalysts by encapsulating Pt nanoparticles in self-assembled silica nanostructures [4, 5].
To be able to understand the mechanisms behind the self-assembly process of nanoparticles (NP), it's necessary to understand the intermolecular forces that act between the particles. Therefore, the following sections will concentrate on the inter-particle interactions and the current state of research on NP monolayer self-assembly.

2.1.1 Current State of Research on Nanoparticle Self-Assembly

Nanomaterials can be created through two main approaches: top-down and bottom-up methods. In top-down methods, bulk materials are broken down into nanoscale structures through physical or chemical processes. Common methods include mechanical milling, thermal evaporation, laser ablation, and sputtering. Top-down methods can synthesize more complex particle morphologies, but are restricted by size limitations and difficulties in achieving industrial scalability due to high operational costs [6]. Conversely, bottom-up approaches permit the construction of nanostructures through the synthesis of nanoparticles from atomic or molecular levels with more precise control and lower costs. Recently, self-assembled monolayers of colloids created through bottom-up processes have attracted particular attention. These can be categorized according to their applications, which include cases where the monolayer and its intrinsic properties are of interest, and cases where the monolayer functions as a mask or modulating substrate, facilitating the deposition of other materials. The latter application serves as the fundamental principle underlying Nanosphere Lithography [7].
A variety of methods to fabricate NP monolayers on a solid substrate from NP dispersion are known. Notable methods are: dip-coating, spin-coating, drag-coating, and drop-casting. Dip-coating (Fig. 2.1a) involves the deposition of NPs onto a clean, solid substrate by vertically holding it into the NP dispersion. Afterwards, the substrate can either be removed or kept stationary, while the liquid is either slowly drained or evaporates. Linear, continuous growth of the particle monolayers can be achieved via the convective transfer

of particles due to the liquid evaporation from the film surface and interparticle and substrate particle interactions [7]. An application of this technique is demonstrated by Su et al. (2020), who developed an annealing-assisted dip-coating method to synthesize 10 nm magnetite (Fe_3O_4) NPs and graphene on carbon cloths. The aim is to construct high-performance electrodes for flexible superconductors. [8]

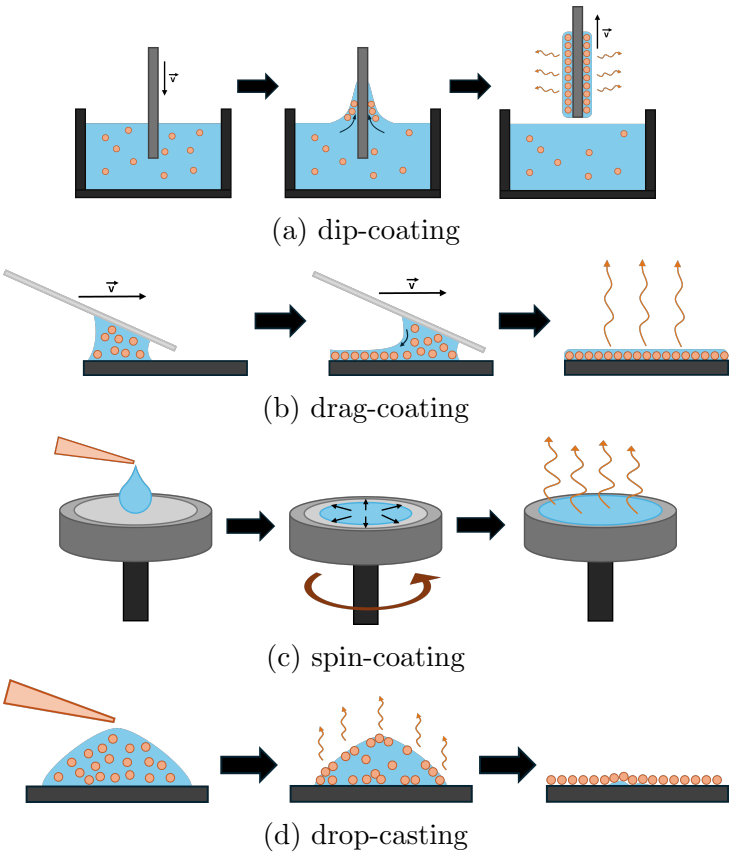

(a) dip-coating

(b) drag-coating

(c) spin-coating

(d) drop-casting

Figure 2.1: Schematic diagram of differing self-assembly processes: a) dip-coating, b) drag-coating, c) spin-coating, d) drop-casting. These methods by allowing the solvent to evaporate as a final step.

A comparable method to dip-coating is called drag-coating (Fig. 2.1b), which entails horizontally dragging a drop of NP dispersion across a flat substrate using a blade. The dominant forces responsible for self-assembly are analogous to those observed in dip-coating, although the horizontal and

vertical convective forces depend on the surface curvature of the drop and the contact angle between the blade and substrate [7, 9]. Chen et al. (2024) a one-step liquid-surface drag-coating method to fabricate organic memory devices. The method involves creating a bilayer structure by spreading a solution containing organic semiconductors and insulating polymers across a water surface, that is then transfered to a substrate. [10]

Spin coating (Fig. 2.1c) is a process in which a drop of NP dispersion is deposited onto the center of the substrate and the substrate is spun at a certain rotational speed to allow the liquid droplet to spread over the substrate. It is a simple, rapid, and suitable method for large-area self-assembly. It is necessary to exercise caution when adjusting spinning protocols, particularly with regard to spinning speed and acceleration rate. Additionally, it is important to control several parameters, such as particle concentration and droplet volume, in order to achieve more optimal assemblies of nanoparticles [7]. Barzinij et al. (2020) fabricated zinc oxide (ZnO) thin films by spin-coating 60 nm ZnO NPs on silicon wafers. Afterwards, the films were annealed at high temperatures to achieve crystalline ZnO thin films. [11]
An alternative method is drop casting (Fig. 2.1d), which deposits NPs on a flat substrate. The NP self-assembly begins with the evaporation of the solvent, causing the NPs to fall into ordered structures. This approach is straightforward but challenging to control due to the complex mechanisms involved in solvent evaporation. The main mechanisms are evaporation-driven radial flow, mangoniflow, and interparticle forces. During the evaporation process, the solvent tends to evaporate more rapidly towards the edges than towards the center of the droplet. This results in a greater loss of solvent at the edges, which is then compensated by an edgeward radial flow of the solvent and the particles dispersed in it, from the center towards the edges. Consequently, particles tend to agglomerate at the edges, leading to the coffee ring effect. Furthermore, the evaporation process generates latent heat and results in an uneven cooling of the drop surface, which gives rise to a surface temperature gradient. In general, there is an inverse relationship between temperature and surface tension, with surface tension decreasing as temperature increases. This effect gives rise to a Marangoni flow throughout the drop, which creates a flow from the top of the surface down to the substrate. At this point, NPs either adsorb to the substrate surface or continue to flow towards the drop edges [7]. The interparticle forces, particularly the combined capillary force effects between particles, can be influenced by adjusting the pH, adding surfactants, controlling the NP concentration and

overall drop volume, selecting an appropriate solvent, and controlling the environment of the self-assembly process. For instance, the addition of stearyl alcohol has been found to be effective in improving the long-range NP order, in addition to annealing the system after solvent evaporation [12].

2.1.2 Particle Interactions

Interparticles forces are the main drivers of bottom-up nanoparticle assemblies, which describe the forces acting between neighboring particles and determine the collective behavior of a system comprised of nanoscale particles. They are generally weaker than the intraparticle forces, which responsible for holding a single particle together and determining the chemical and physical properties of a material.

Van der Waals Force (version 1 - longer version, shorter see below)
written very nice but quit long. For me, it is fine but i don't know about Oleg???
The self-assembly of NP is generally driven by non-covalent interactions such as the van der Waals (vdW) force, which is regarded as the weakest of the chemical forces with a short range. It is considered a fundamental force for self-assembly and is divided into three types: the Keesom force (orientation force), Deby force (induction force), and London dispersion force.
The Keesom force defines dipole-dipole interactions between particles with permanent electric dipoles where their attraction stems from oppposite partial charges. The strength of this force is influenced by the orientation of the particles, which is why it is also known a an orientation-dependent force. The Keesom interaction energy is described by:

$$E = -\frac{2}{3k_BT}\left(\frac{p_1p_2}{4\pi\varepsilon_0\varepsilon_r}\right)^2\frac{1}{r^6}$$

where p is the electric dipole moment, k_B is the Boltzmann constant, T is the temperature, ε_0 is the electric constant, ε_r is the relative permittivity, and r is the particle-to-particle distance.
The Debye force describes the interaction between a permanent dipole and an induced dipole. A particle with a permanent dipole induces a dipole in a neighboring particle, therefore causing a charge dislocation within by distorting its electron cloud density. The Debye force is also called the induction force and its interaction energy is written as:

$$E = -\frac{p^2\alpha'}{4\pi\varepsilon_0\varepsilon_r}$$

α' is the polarizing volume and is expressed as $\alpha' = \frac{\alpha}{4\pi\varepsilon_0\varepsilon_r}$ with α being the polarizability.

The London dispersion force refers to interactions between two particles with spontaneously induced dipoles and occur between all atoms, molecular, and particles, regardless of polarity. The forces result from random fluctuations in electron distributions that cause temporary dipole moments in a particle. The following equation describes the London dispersion interaction:

$$E_{12}^{disp} = -\frac{3}{2}\frac{\alpha_1'\alpha_2'}{r^6}\frac{I_1 I_2}{I_1 + I_2}$$

where I_n is the ionization energy.

Out of these three types of vdW interactions, the Keesom force is considered to be the strongest in terms of relative strength, while the London dispersion force is the weakest. However, the dispersion force plays a major role in NP self-assembly and comprises most of the vdW interactions [13]. The vdW interactions can be calculated for nanoparticles assemblies by use of the Dzyaloshinkskii-Lifshitz-Pitaevskii (DLP) theory and applying the Derjaguin appromixation depending on the NP morphology and chemical characteristics. For spherical particles with a smooth surface in particular, the dispersion potential can be approximated by the Hamaker approach:

$$E_{vdW} = -\frac{A_H}{6}\left[\frac{2R_1R_2}{h(h+2R_1+2R_2)} + \frac{2R_1R_2}{(h+2R_1)(h+2R_2)} + ln\left(\frac{h(h+2R_1+2R_2)}{(h+2R_1)(h+2R_2)}\right)\right]$$

with h being the particle distance and A_H the Hamaker constant. This equation can be simplified by applying the Derjaguin approximation, which is used to estimate the interaction energy between curved surfaces as a function of the distance between them [14]:

$$E = -\frac{A_H}{6}\left(\frac{R_1R_2}{R_1+R_2}\right)\frac{1}{h}$$

The vdW interactions are the primary attractive forces in self-assembly processes driven by solvent evaporation, where NP organize into ordered structures. As the solvent evaporates, the NP concentration gradually increases, which in turn increases the interparticle energy between the particles. This induces NP assembly through the interparticle forces, which often counteracts against electrostatic and stearic repulsion [13]. By controlling the solvent evaporation conditions like the solvent, temperature and evaporation rate, the assembly structure can be influenced.
The thermodynamic principles during solvent evaporation-induced assembly processes can be described as a balance between configurational- and free volume entropy. The configuration entropy describes the number of ways NPs can be arranged in a defined region. A high entropy indicates a disordered system with many possible configurations, while a low entropy points to a more ordered structure with fewer possible configurations for NPs. The free volume entropy is associated with the available free space for translational and rotational movements of particles. Ordered structures may increase free space on a substrate, which in turn increases the free volume entropy. As the solvent evaporates, the NPs assemble into organized structures, reducing configuration entropy while free volume entropy increases. This makes the self-assembly process energetically favorable by lowering the system's energy and increasing its entropy. [13]

Van der Waals Force (version 2 - shorter version)
The self-assembly of NP is generally driven by non-covalent interactions such as the van der Waals (vdW) force, which is regarded as the weakest of the chemical forces with a short range. It is considered a fundamental force for self-assembly and is divided into three types: the Keesom force (orientation force), Deby force (induction force), and London dispersion force.
The Keesom force defines dipole-dipole interactions between particles with permanent electric dipoles where their attraction stems from oppposite partial charges. The strength of this force is influenced by the orientation of the particles, which is why it is also known a an orientation-dependent force.
The Debye force describes the interaction between a permanent dipole and an induced dipole. A particle with a permanent dipole induces a dipole in a neighboring particle, therefore causing a charge dislocation within by distorting its electron cloud density. It is also called the induction force. The London dispersion force refers to interactions between two particles with

spontaneously induced dipoles and occur between all atoms, molecular, and particles, regardless of polarity. The forces result from random fluctuations in electron distributions that cause temporary dipole moments in a particle. The following equation describes the London dispersion interaction:

$$E_{12}^{disp} = -\frac{3}{2}\frac{\alpha_1'\alpha_2'}{r^6}\frac{I_1 I_2}{I_1 + I_2}$$

where I_n is the ionization energy.
Out of these three types of vdW interactions, the Keesom force is considered to be the strongest in terms of relative strength, while the London dispersion force is the weakest. However, the dispersion force plays a major role in NP self-assembly and comprises most of the vdW interactions [13]. The vdW interactions can be calculated for nanoparticles assemblies by use of the Dzyaloshinkskii-Lifshitz-Pitaevskii (DLP) theory and applying the Derjaguin appromixation depending on the NP morphology and chemical characteristics. For spherical particles with a smooth surface in particular, the dispersion potential can be approximated by the Hamaker approach. This can be simplified by applying the Derjaguin approximation, which is used to estimate the interaction energy between curved surfaces as a function of the distance between them [14]:

$$E = -\frac{A_H}{6}\left(\frac{R_1 R_2}{R_1 + R_2}\right)\frac{1}{h}$$

The vdW interactions are the primary attractive forces in self-assembly processes driven by solvent evaporation, where NP organize into ordered structures. As the solvent evaporates, the NP concentration gradually increases, which in turn increases the interparticle energy between the particles. This induces NP assembly through the interparticle forces, which often counteracts against electrostatic and stearic repulsion [13]. By controlling the solvent evaporation conditions like the solvent, temperature and evaporation rate, the assembly structure can be influenced.

Electrostatic force

Electrostatic interactions are long-range forces between particles with electric charges that can be attractive or repulsive. In colloidal dispersions, particles may gain surface charges that cause electrostatic repulsion between them. This prevents nanoparticles (NPs) from agglomerating or coagulating and

stabilizes the dispersion. The induced electric charges can be influenced by controlling the pH of the dispersion, thereby changing the electrostatic interactions. By designing NPs with specific electric charges, directing the assembly process is made possible to form new nanomaterials [13].

Steric Repulsion

To overcome the aggregation of nanoparticles (NPs) inside a liquid due to attractive van der Waals (vdW) or dipolar interactions, there should be some kind of repulsive force. One such repulsive force is steric repulsion. This force is based on the Pauli exclusion principle, which comes into effect when charge distributions of atoms overlap. In combination with electrostatic effects, steric repulsion is used to prevent the aggregation of nanoparticles in dispersion and counterbalances the effects of attractive vdW forces. The aforementioned phenomenon can be influenced by modifying particle surfaces through the adsorption of a surfactant or by attaching ligands whose free ends repel each other [15].

Capillary Forces

Capillary forces are a phenomenon that occurs during interactions between liquid and solid interfaces. These forces can be divided into two categories: adhesive forces between dissimilar materials and cohesive attraction between similar particles or molecules. Attractive capillary forces originate from adhesive forces between liquids and closely neighboring particles, as well as the formation of cohesive liquid bridges between them. Due to surface tension, these bridges develop curved surfaces that cause a pressure difference called Laplace pressure. This pressure difference across the curved liquid interface results in attractive capillary forces that pull neighboring particles together [16].

2.2 Silica Nanoparticles

Silica nanoparticles (NPs) have gained interest in a range of applications due to their low toxicity and good biocompatibility. In addition to being able to be synthesized over a wide size range, they can be inexpensively created using various methods [17]. Consequently, silica nanoparticles (NPs) are

employed in a multitude of fields, including biomedicine and technology, cosmetics, the food industry, semiconductors, and environmental applications for purifying water by removing contaminants such as oil, heavy metals, and radioactive materials [18]. The most prevalent methods for synthesizing silica NPs are wet chemical methods, sol-gel processes, ultrasonication, dry synthesis, and reverse microemulsion [19]. Silica nanoparticles can be prepared with good monodispersity, possess a low Hamaker constant, which reduces van der Waals forces between particles in self-assembly [12], and are very stable in solutions [20]. Additionally, the surface of silica nanoparticles is covered with silanol groups, which facilitate extensive surface modifications. Recently, mesoporous silica with tunable pores has attracted attention for improving drug loading capacities in biomedical applications [21].

2.3 Scattering

Scattering is the redirection of radiation (light, X-ray, electron, neutron, etc.) out of the original direction of propagation due to interactions with another object. Scattering techniques are powerful tools for materials science, as they can reveal statistically-averaged structural information (structure, composition, etc.). In this thesis, X-ray scattering methods, including small-angle X-ray scattering (SAXS), grazing-incidence small-angle X-ray scattering, and X-ray reflectivity, are employed to investigate the structural arrangement of silica nanoparticle assemblies. The following sections provide a detailed explanation of these methods.

2.3.1 Scattering Theory

During X-ray scattering, X-ray beams impinge upon a sample as an incoming wave $\vec{k_i}$, which interacts with the sample, and subsequently scatters away in different directions as an outgoing wave $\vec{k_f}$. The scattering angle, denoted by θ, represents the angle between the incident and scattered vectors (Fig. 2.2). The difference between these vectors, referred to as the momentum transfer, is the scattering vector $\vec{q}$ and is expressed as: [22]

$$\vec{q} = \vec{k_f} - \vec{k_i}$$

For elastic scattering, the magnitude of $\vec{q}$ quantifies the momentum transfer between $\vec{k_i}$ and $\vec{k_f}$ and can be calculated by:

$$|\vec{q}| = \sqrt{k_i^2 + k_f^2 - 2k_i k_f \cos(2\theta)} = \sqrt{2k^2(1 - \cos(2\theta))} = \frac{4\pi}{\lambda}\sin(\theta)$$

where λ is the X-ray wavelength and $|\vec{k_i}| = |\vec{k_f}| = k = \frac{2\pi}{\lambda}$. Each q-value (momentum transfer in reciprocal-space) corresponds to a real-space distance d and can be calculated using $q = \frac{2\pi}{d}$.

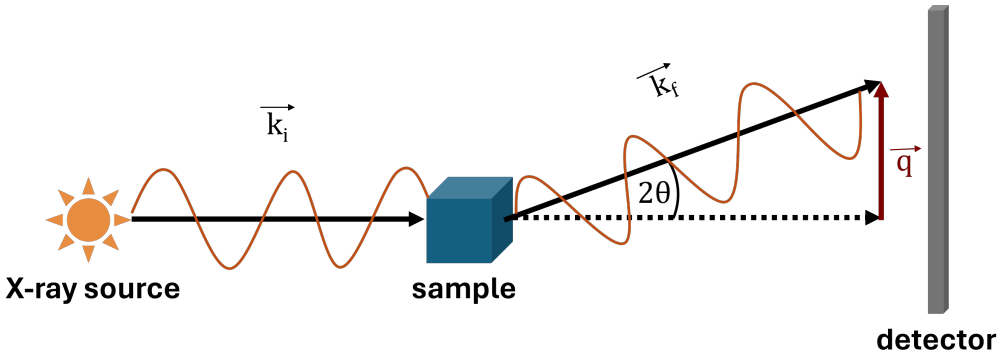

Figure 2.2: Schematic of X-ray scattering, depicting $\vec{k_i}$ as the incoming wave, $\vec{k_f}$ as the outgoing wave after interacting with a sample, and $\vec{q}$ as the scattering vector. The waves of $\vec{k_f}$ are then collected by a detector.

The scattering process results in the formation of scattering patterns, which are subsequently captured by a detector. The scattered waves either interfere constructively or destructively. Constructive interference occurs when the waves are moving in phase with each other, and it is defined by Bragg's Law:

$$n\lambda = 2d\sin(\theta)$$

with the diffraction order n and the interlayer distance d. Sharp intensity spikes are known as Bragg peaks and observed at specific angles where Bragg's Law is satisfied. They provide information about regular structures occurring within a sample. The scattering intensity $I(\vec{q})$ in the reciprocal space in general is linked to the spatial distribution of the scattering matter

and is the Fourier transform of the density distribution of a sample. It signifies the transformation of the position-based information of the real space to the momentum-based information of the reciprocal space, as it is a function of the scattering vector $\vec{q}$. The density distributions directly influence X-ray scattering intensity described as: [22]

$$I(\vec{q}) = \left\langle \left| \sum_{n=1}^{N} \rho_n e^{i\vec{q}\cdot\vec{r}_n} \right|^2 \right\rangle$$

the sum of the scattering contributions of all scattering objects N and their scattering power ρ_n and can be written as an integral form for a continuous distribution of the scattering density $\rho(\vec{r})$ over the real space:

$$I(\vec{q}) = \left| \int_V \rho(\vec{r}) e^{i\vec{q}\cdot\vec{r}} dV \right|^2$$

where the inner component is known as the form factor $F(\vec{q})$ and is mathematically identical to the Fourier transform [22]:

$$I(\vec{q}) = |F(\vec{q})|^2, \quad F(\vec{q}) = \int \rho(\vec{r}) e^{i\vec{q}\cdot\vec{r}} dV$$

The form factor $F(\vec{q})$ describes how the size and shape of the individual scatters within a sample influences the scattering intensity. However, when the objects within the sample cannot be considered isolated, but occur in structures where they are correlated with each other, it's necessary to include an additional spatial component denoted as the structure factor $S(\vec{q})$. For nanoparticle systems with N identical particles, $S(\vec{q})$ is defined as:

$$S(\vec{q}) = \frac{1}{N} \left| \sum_{n=1}^{N} e^{i\vec{q}\cdot\vec{r}_n} \right|^2$$

and provides information about nanoparticle ordering and correlation between ordered domains.
By using the orientational average of the form factor $F(q) = |F(\vec{q})|^2$, the scattered intensity including $S(\vec{q})$ is expressed as: [23]

$$I(q) = \langle |F(\vec{q})|^2 S(\vec{q}) \rangle = F(q)S(q)$$

2.3.2 Small-Angle X-ray Scattering (SAXS)

Small-angle scattering (SAS) is a method used to study structure and interactions of systems with the size on the order of 10 to 1000 Å. This is achieved by illuminating the sample with either X-rays or neutron sources. In this thesis, only small-angle X-ray scattering (SAXS) is used to gain information about the shape, size and size distribution of nanoparticles. In this case, the scattering intensity is measured in transmission geometry, as the samples are usually dispersed in a solvent. A collimated beam is focused onto the sample at small angles of $2\theta = 0.1^\circ$ - 10°, then scattered by the scattering objects in the dispersion and captured by a detector (Fig. 2.3a). During this process, X-rays interact with the electron clouds of the sample's atoms, causing the electrons to oscillate and redirect the X-rays in different directions (Fig. 2.3b). The scattering patterns and intensity depend on the size, shape and material properties of the scattering objects. Since this process occurs through elastic scattering, the X-ray wavelength does not change. The degree to which a material scatters X-rays is dependent on its electron density. Consequently, heavier atoms will scatter X-rays with greater intensity than lighter atoms. This phenomenon is quantified by the Scattering Length Density (SLD), which is defined as the sum of the scattering lengths (b_n) of a given number of atoms (n), divided by the volume (V) occupied by those atoms:

$$SLD = \frac{\sum_{i=1}^{N} b_n}{V}$$

Knowing the SLD is useful in determining electron density variations within a sample, as higher density variations lead to higher SLD variations, which gives insight into the composition of complex systems with different materials and phases.

For nanoparticles speficially, the analysis of SAXS measurements starts with form factor analysis, which generally assumes a specific physical form and mathematically fits models of particle shapes onto the experimental SAXS data. For this, low-q data is is primarily used to determine the overall size and shape by use of Guinier analysis:

$$I(q) = I(0)e^{-\frac{1}{3}R_g^2 q^2}$$

with R_g being the radius of gyration, which provides quantifies the particle size. Particles with geometrically shapes such as spheres with radius R and

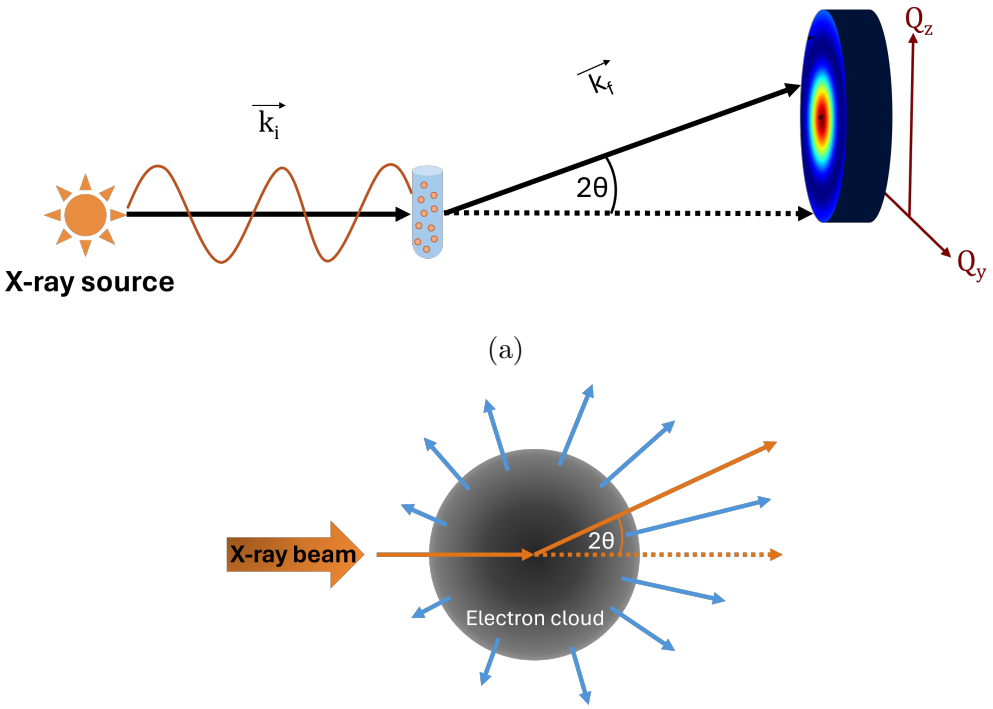

Figure 2.3: Schematic of the SAXS geometry: a) collimated X-ray beams are scattered at an angle 2θ by a sample dispersed in a solution, then captured by a detector. The resulting SAXS image measures the intensity of the scattered beams as a function of (Q_y, Q_z). b) During SAXS, the sample's electron cloud redirects the X-ray path into different directions.

volume $V = \frac{4\pi}{3}R^3$ have a form factor:

$$F(q) = \Delta SLD \, \frac{3(\sin(qR) - qR\cos(qR))}{(qR)^3} V$$

in which $\Delta SLD = SLD_{particle} - SLD_{Solvent}$. If R_g corresponds to $R_g = R\sqrt{5}$ with R determined by form factor analysis, it is highly likely that the particles in the measured dispersion are of spherical shape. [22, 23]

2.3.3 Grazing-Incidence Small-Angle X-ray Scattering (GISAXS)

Grazing-incidence small-angle X-ray scattering (GISAXS) is a surface-probing technique to study the in-plane lateral structure of nanostructures and thin films. It is derived from the principles of SAXS measurements with the key difference being that its setup uses reflection geometry. The incoming X-rays, with wavevector k_i are emitted at very shallow angles α_i close to 0° and graze the sample surface, reflecting off it and scattering along k_f in the direction $(\alpha_f, 2\theta_f)$. The scattered X-rays are collected by a 2-D detector, which measures specular and off-specular scattering to gain information about the surface structure. GISAXS measurements produce 2-D images in Q_y and Q_z direction with the general geometry (Fig. 2.4) described by:

$$\vec{q}_{x,y,z} = k \begin{pmatrix} \cos(2\theta_f)\cos(\alpha_f) - \cos(\alpha_i) \\ \sin(2\theta_f)\cos(\alpha_f) \\ \sin(\alpha_f) + \sin(\alpha_i) \end{pmatrix} \tag{2.1}$$

with $k = \frac{2\pi}{\lambda}$ where λ is the wavelength and $\vec{q} = \vec{k_f} - \vec{k_i}$. [24]

When specular reflectivity occurs, following conditions are fulfilled: $\alpha_i = \alpha_f$, $2\theta = 0$, $Q_x = Q_y = 0$, and $Q_z \neq 0$. This enables the calculation of the incident angle at which the GISAXS measurement has been performed by obtaining the q_z-position of the specular reflection and using $q = \frac{4\pi}{\lambda}\sin(\alpha)$. At $\alpha_i \neq \alpha_f$ and $2\theta = 0$, off-specular reflection occurs and gives insights into the surface roughness of the sample. The scattering patterns occuring at $\alpha_i \neq \alpha_f$ and $2\theta \neq 0$ contain information about the global lateral structures and the in-plane lateral ordering.
Generally, X-rays do not interact strongly with matter, which leads to the X-ray refractive index being slightly less than 1, which gives rise to total external reflection at sufficiently small angles. Consequently, when the incident angle of the X-ray beam is below the critical angle α_c ($\alpha_i < \alpha_c$), total external reflection occurs.
Measuring at the material-dependent critical angle α_c leads to the refracted X-ray beam being nearly parallel to the sample surface and gives rise to X-ray standing wave effects. The X-ray beam travels as an evanescent wave through the surface plane of the sample, which increases the path length of the beam through the surface to its maximum. This leads to scattering signals with the highest obtainable intensities for the sample. Consequently,

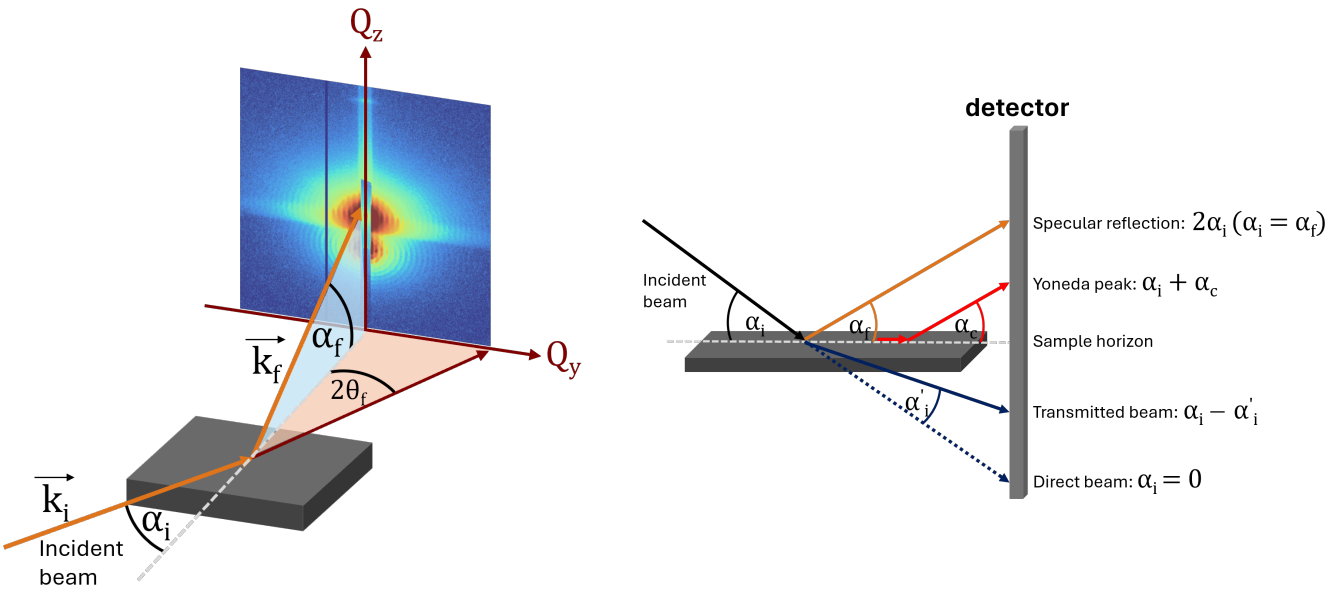

Figure 2.4: Schematic of the GISAXS geometry: a) the general geometry with reciprocal axes. b) schematic of the different scattering events during GISAXS

measuring at the critical angle is beneficial in enhancing the contrast and sensitivity of GISAXS data, thereby facilitating the characterization of surfaces of nanostructures.
An incident angle above the critical angle ($\alpha_i > \alpha_c$) of total reflection lets the X-ray beam penetrate deeper into a sample as a transmitted beam with $\alpha_i^{'}$ and increases depth sensitivity of the GISAXS data. This is useful in probing both surface layers and sub-surface structures. [24]

2.3.4 X-ray Reflectivity (XRR)

X-ray Reflectivity is a method to investigate the surface roughness, thickness and density of thin films and multilayers. The basic principle underlying XRR is reflecting a X-ray beam off the sample surface and measuring the intensity of the reflected beam. The intensity of the reflected beam is measured as a function of the incident angle θ_i where $\theta_i = \theta_f$, which is by definition specular reflectivity. The scattering vector is parallel to the z-axis as the surface normal, reducing the momentum transfer to a one dimensional

problem:

$$Q_z = \frac{4\pi}{\lambda} \sin(\theta)$$

When the X-ray beam hits the sample surface, both reflection and refraction occur (Fig. 2.5).

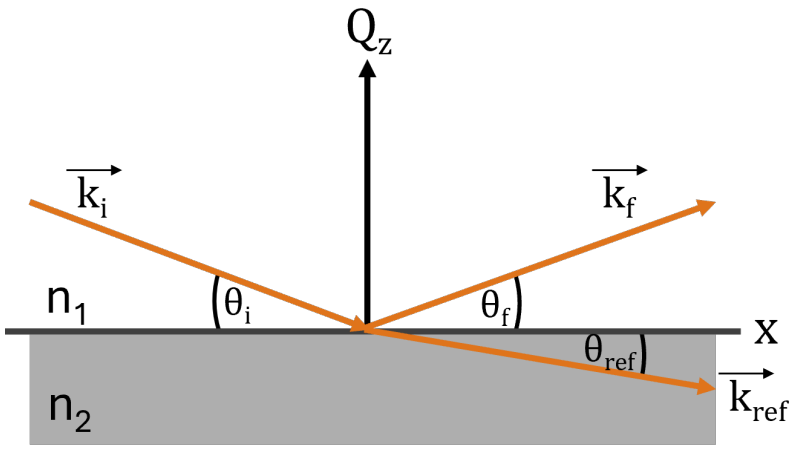

Figure 2.5: Schematic of the XRR geometry

The relation between incident and refracted beam is described according to Snell's law:

$$n_1 \sin(\theta_i) = n_2 \sin(\theta_{refracted})$$

Since the refractive index for materials during X-ray interactions are slightly below 1, total external reflection of the X-rays occurs at incident angles equal to or below the critical angle ($\theta_i \leq \theta_c$).
At an ideal surface with a single interface, the reflected intensity R can be calculated using Fresnel equations:

$$R_f = |r|^2 = \left| \frac{k_{z,i} - k_{z,refracted}}{k_{z,i} + k_{z,refracted}} \right|^2$$

$k_{z,i}$ and $k_{z,ref}$ are the vertical components of the incident and transmitted beam, respectively. [25]
When the sample has multiple interfaces, oscillations in the XRR curve

known as Kiessig fringes appear. Kiessig fringes result from the interference of X-rays reflected from different interfaces in the sample. The phase difference $\Delta\phi$ of the reflected beam at the top and bottom of the interface with layer thickness d is given by:

$$\Delta\phi = \frac{4\pi}{\lambda} d \sin(\theta)$$

Constructive interference occurs when the phase differences are multiples of 2π leading to the condition described by Bragg's law:

$$d = \frac{n\lambda}{2\sin(\theta)}$$

The layer thickness can be calculated by using the relation:

$$d = \frac{2\pi}{\Delta Q_z}$$

and using $\Delta Q = \frac{4\pi}{\lambda}\Delta \sin(\theta)$, where ΔQ is the spacing in Q between the fringes. [25]

Chapter 3

Experimental Methods and Instruments

This chapter briefly introduces the method for sample preparation and the characteristics of all instruments used for investigations.

3.1 Sample Preparation

3.1.1 Synthesis of silica nanoparticles

The silica NPs used in this study were obtained in collaboration with Dr. Johan Buitenhuis from the Institute for Biomacromolecular Systems and Processes (IBI-4) at Forschungszentrum Jülich. Monodisperse silica particles were synthesized using the microemulsion method [26–28]. Particles with a diameter of approximately 200 nm were obtained using ethanol as a solvent. Concentrations are expressed as volume fractions, calculated using the densities of the solvent and silica assuming additivity of volumes. The silica particles were assumed to have an average density of 1.8 g/ml, which is consistent with the density measurement of formed silica colloids of similar size. According to the described synthesis process, a stock dispersion of colloidal particles containing 5.4 vol% silica nanoparticles was prepared. The particles were stored in a sealed bottle in a refrigerator. They have a shelf life of more than two years, after which they might begin to degrade.

3.1.2 Nanoparticles dispersion for monolayer formation

A colloidal dispersion with 5.4 vol% silica nanoparticles in Ethanol was prepared as stock. Additionally, we prepared a stock solution of stearyl alcohol in ethanol with a concentration of 5.4 vol%. These two stock solutions were used to create a highly ordered multilayer structure on a silicon substrate using the drop-casting technique by controlling the aggregation process. To improve the ordering of NPs across the entire sample area, we used stearyl alcohol as an assistant. Next, a solution containing 0.1 vol% silica and 0.1 vol% stearyl alcohol was created by adding 20 μL of 5.4 vol% silica and 20 μL of 5.4 vol% stearyl alcohol to 0.96 mL of Ethanol.

3.1.3 Drop-Casting

The substrate for NP deposition was N-type Si (100) wafers obtained from Crystec GmbH. The wafers have a thickness of 0.5 mm and were cut into pieces of 10 $\times$ 10 mm^2. Prior to deposition, they were sonicated in an Elmasonic P60 ultrasonic bath using ethanol and distilled water (DI), respectively, to remove dust particles and contamination from the substrate surface. Finally, the substrates were stored in ethanol for future use. After applying the aforementioned treatment, NPs were deposited on the substrates using the drop-casting method, which will be explained in detail later.
The nanoparticles were deposited onto the cleaned silicon substrate using an improved variant of the drop-casting technique, which is simple, inexpensive, and requires no additional equipment. In this method, a certain volume of NP dispersion is dropped onto the silicon substrate, where it assemblies in various thicknesses. The morphology of the NP assemblies obtained using this method depends on the solvent evaporation rate and the amount of NP dropped on the substrate. Several parameters can be controlled, such as the use of an appropriate concentration of NP and stearyl alcohol and an appropriate drop volume, to improve the degree of ordering of the NPs using the drop-casting method [12]. The method is schematically depicted in figure (). To determine the ideal drop volume for the preparation of highly ordered multilayers of silica nanoparticles with a diameter of about 200 nm over a large area on a silicon substrate by an improved variant of the drop-casting method, we performed a drop volume series investigation. The silicon wafers were cleaned and placed in individual Petri dishes, and the nanoparticle dis-

persion was drop-cast onto the substrate using a micropipette. The drop volume was varied from 5 μL to 40 μL in increments of 5 μL. This resulted in 8 samples. The Petri dishes were then covered with parafilm to reduce the evaporation rate of ethanol and thus increase the time for the nanoparticles to self-assemble into ordered monolayers. The sample preparation was conducted in a clear, open polystyrene chamber at room temperature

3.1.4 Annealing Process

After the appropriate volume of the solution was dropped into the silicon substrate and the solvent was allowed to completely evaporate, the sample was left to dry overnight. Subsequently, it was heat-treated in an oven to reduce the number of cracks and other defects observed in the formed multilayers (see section 4.2). The samples were annealed above the melting temperature of stearyl alcohol (59.5°C [29]), which is a solid at room temperature. This will cause the stearyl alcohol in the formed multilayers to melt during this additional step, allowing the particles to move freely and self-assemble further, resulting in a multilayer with improved order [1]. Samples were annealed in an oven at 70°C for 10 days in a clear polystyrene sample container. Grains of stearyl alcohol were added to the sample to create a stearyl alcohol environment.

3.2 Scanning Electron Microscope (SEM)

Scanning Electron Microscopy (SEM) is a method for characterizing samples by scanning their surfaces with a high-energy focused electron beam to produce direct space images of the sample with a resolution in the nm range. The Hitachi Model SU8000 Field Emission Scanning Electron Microscope at PGI-7 (Peter Grünberg Institute for Electronic Materials) institute was used for SEM imaging. The schematic for the instrument is pictured in Fig. 3.1. An electron beam is generated by an electron gun, which uses a cold cathode field emission source with a mono-crystalline tungsten tip. An electric field is applied to lower the work potential until the point where electrons can tunnel through the tungsten tip is reached. The electrons are then vertically emitted through the evacuated chamber and accelerated with a voltage of 0.5 – 30kV. A three-stage electromagnetic lens system is used to control the path of the electron beam and collimate it, while a gun valve placed in be-

tween the optics regulates the electron flow. The electron beam first passes through two condenser lenses that demagnify the beam while the objective lens focuses the beam on the sample. A set of electromagnetic deflection coils then generates a magnetic field that deflects and steers the electron beam and facilitates raster scanning across the sample surface. The sample itself is placed on a sample stage in the sample chamber and its surface can be magnified in two modes, the low mode with a magnification of (20x - 2.000x) and the high mode with a magnification of (80x - 800.000x).

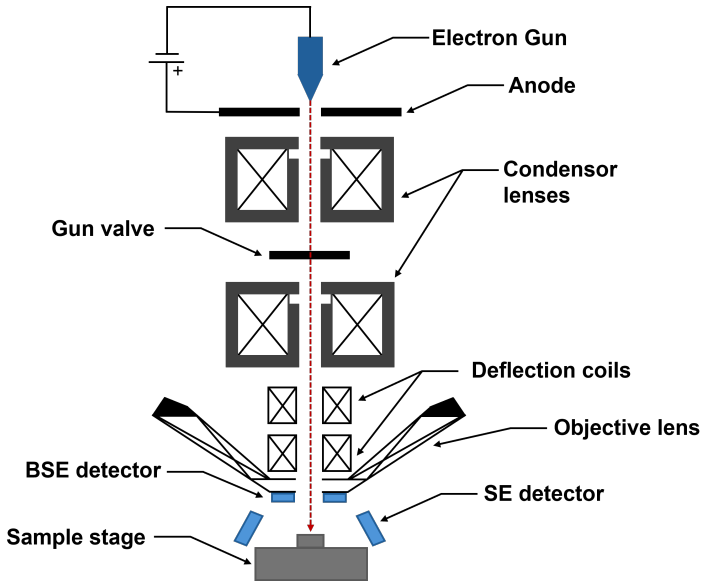

Figure 3.1: Schematic of the Scanning Electron Microscope

When the electron beam reaches the sample surface, various signals are produced (Fig. 3.2. The signals mainly used stem from either elastic or inelastic scattering of the incident electrons of the emitted beam. When inelastic scattering occurs, incident electrons cause the ionization of sample atoms which results in outer shell electrons to be emitted from the sample atom. These are called secondary electrons (SE) and typically possess a low energy of around 3 – 5eV [30]. Due to their low energy, the only SE able to escape from the sample are those near the sample surface, since those produced in deeper regions tend to get reabsorbed into the sample. This also results in a lateral resolution of around 10nm which is suitable for obtaining high-resolution images of the sample surface. A SE-detector placed in the lower region of the

device collect the scattered SE and transmit the signal to a monitor. The SE signals are primarily used in this thesis and needed to obtain local surface information of the samples.

When incident electrons instead scatter elastically within the sample and can escape from the sample surface, they typically emerge from deeper within the sample. These electrons are called back-scattered electrons (BSE) and have energies higher than 50eV and a lateral resolution of 1μm [30]. Therefore, BSE signals are usually used to gather information of sample characteristics from deep below the surface and can prob the specimen composition due to the sensitivity to differences in atomic number.

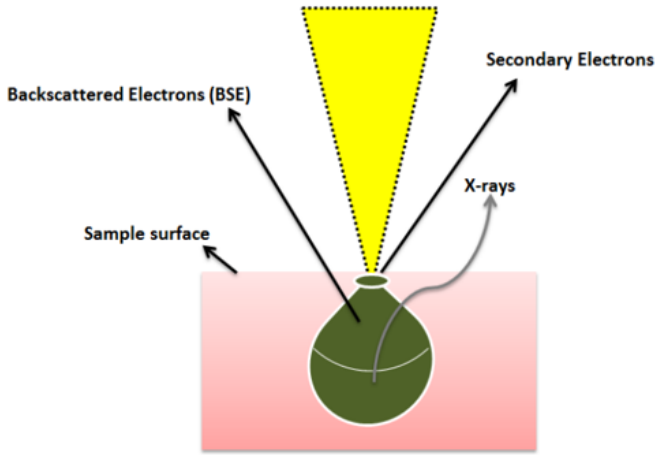

Figure 3.2: Schematic of the differeny types of signals emitted during a SEM measurement. [31]

3.3 Gallium Anode Low-Angle X-ray Instrument (GALAXI)

The JCNS GALAXI (Gallium Anode Low-Angle X-ray Instrument) diffractometer at Forschungszentrum Jülich, is a high brilliance laboratory small-angle X-ray scattering instrument [32]. Fig. 3.3 shows the instrument's schematic. Small Angle X-ray Scattering (SAXS) and Grazing Incidence Small Angle X-ray Scattering (GISAXS) have been performed at GALAXI.

A Metaljet source by Bruker AXS is used as the X-ray source that uses a liquid metal jet of a GaInSn alloy as an anode. It produces Ga K-α radiation with an energy of 9.23 keV and a corresponding wavelength of 1.314 Å. Afterwards, two 4-segment slits S1 and S2 are used to define and collimate the X-ray beam, while the third slit S3 reduces the background. The beam then arrives at the sample position where suitable sample holders can be mounted, depending on the sample and the measurement type. The sample stage can be adjusted by two rotational and two translational degrees of freedom. After the X-ray beam is reflected off the sample surface, the reflected beam travels through the detector tube until it hits the Pilatus 1M 2D detector. The distance between the sample and detector can be varied by adjusting the detector tube length that ranges between 835 mm to 3535 mm in 5 steps. The beam path from the X-ray source to detector is fully evacuated, with pressures reaching less than 1 mbar.

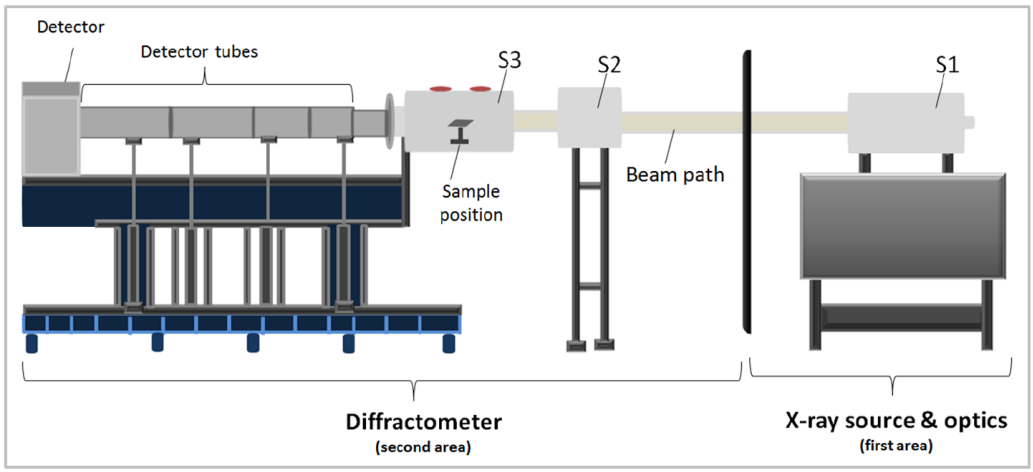

Figure 3.3: Schematic of GALAXI's components [31]

3.3.1 Small-Angle X-ray Scattering (SAXS)

SAXS is a small-angle scattering technique suitable for characterizing the size and shape of particles. The nanoparticle dispersion described in section 3.1.2 is filled into quartz glass capillaries purchased from Hilgenberg GmbH. These capillaries have a diameter of 1.5 mm and a wall thickness of 0.01 mm and are sealed off at the opening with a silicone ball using a silicone gun to allow the

measurement of the dispersion in a vacuum. Next, the capillaries are placed horizontally in a sample holder that can hold up to 11 capillaries and mounted onto the GALAXI sample stage (Fig. 3.4). The sample holder can be moved in the vertical direction to align the sample within the beam path. The capillaries filled with the solvent and the nanoparticle dispersions as well as an empty capillary is measured under the same conditions as a reference sample for the subtraction of the background. SAXS measurements are performed in transmission geometry at two sample-to-detector distances SSSD = 835 mm (short sample detector distance) and LSSD = 3535 mm (long sample detector distance). To determine the beam center and sample-to-detector distance, silver behenate (AgBH) is measured as a reference. Additionally, fluorinated ethylene propylene (FEP) is measured to put the detector count rate into absolute units of cm^{-1}.

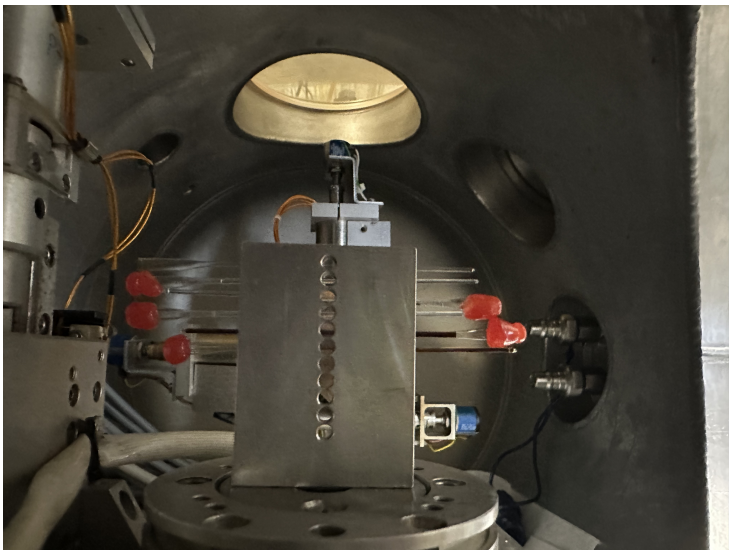

Figure 3.4: Sample holder for SAXS measurements

3.3.2 Grazing-Incidence Small-Angle X-ray Scattering (GISAXS)

Similar to SAXS, Grazing Small Angle X-ray Scattering (GISAXS) also relies on the principles of SAS. However, it is a surface-sensitive method to investigate the surface structure of nanoscale objects. GISAXS measurements

are done in reflection geometry, unlike the transmission-based approach of SAXS. In this setup, the sample is placed in on a flat holder as shown in Fig. 3.5, that can be adjusted with two translational (along y-axes and z-axes) and two rotational (α and β) degrees of freedom as shown in the geometry of the GISAXS experiment. To align the sample with the X-ray beam, the sample holder is moved vertically to center the sample and in the plane to set the beam at the center of the sample. To set the desired angle of incidence, the sample stage is tilted and several scans of the beam transmission are taken while the stage is moved. This centers the sample and ensures that the zero angle corresponds to the flat sample orientation. The incident angle is typically set close to the critical angle (α_c) of the total reflection of the studied material. The samples are measured for a few hours and the data is normalized to the highest monitor count. For analysis of the GISAXS data, the open-source software BornAgain is used to obtain structural information from the collected data. [33, 34]

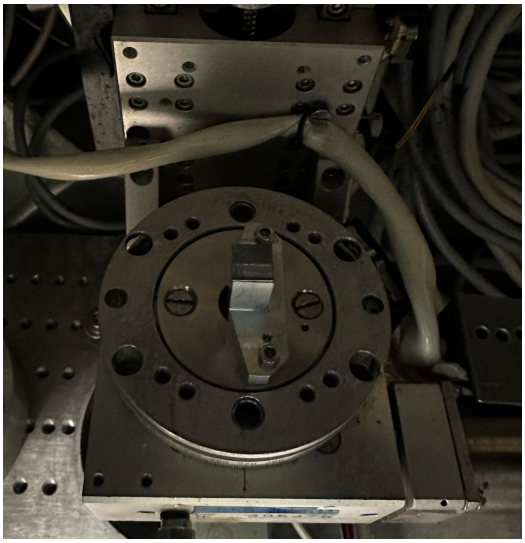

Figure 3.5: Sample holder for GISAXS measurements

3.4 X-ray Reflectivity (XRR)

X-Ray Reflectivity (XRR) is a non-destructive analytical method to determine layer thickness, density and surface or interface roughness using the

effect of total external reflection of X-rays. Here, the Bruker D8 Advance from PGI-7 (Peter Grünberg Institute for Electronic Materials) is used to perform the XRR measurements. A Copper K-α X-ray tube functions as its source with an energy of 8.04 keV, which corresponds to a wavelength of λ = 1.54 Å. The schematic for the instrument is pictured in Fig. 3.6. In this instrument, the X-ray source and detector are mounted on synchronized goniometer arms in a θ:θ configuration, ensuring the incident angle θ_i and the reflected angle θ_r remain equal at all times. At the X-ray source, a Göbel-mirror and two slits S1 and S2 collimate the X-ray beam while an attenuator reduces its intensity to not oversaturate the detector. The beam hits the sample that is placed on a fixed sample stage, where a Knife-Edge-Collimator optimizes the collimation of the incident beam before it is reflected into the detector arm. There, the X-ray beam passes two slits S3 and S4 in addition to another Göbel-mirror and is collected by a detector. The measurements have been performed in a range of $\theta = 0° - 6°$ with a step size of 0.01°, which corresponds to the reciprocal-space range of $Q_z = 0 - 4.27$ nm^{-1}.

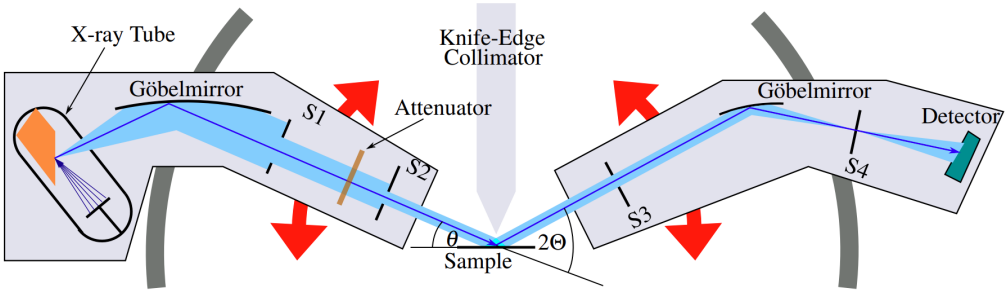

Figure 3.6: Schematic for the XRR instrument [35]

Chapter 4

Results and Discussion

This chapter dicusses the experimental data measured by the aforementioned characterization methods.

4.1 Nanosphere Characteristics and Dispersity

To determine the nanoparticle characteristics and dispersity, Scanning Electron Microscopy (SEM) and Small-Angle X-ray Scattering (SAXS) were performed.
Scanning electron microscopy (SEM) is employed to provide a direct view of the particles and to evaluate the nanoparticle (NP) size and size distribution. For the sample subjected to SEM analysis, a 5μl drop of dispersion with a concentration of 5.4 vol% is transferred to a silicon substrate. The SEM utilized in the subsequent measurements is the Hitachi SU8000, which is described in section 3.2. The diameter of over 150 nanoparticles is manually measured using image processing software, ImageJ [36], from close-up SEM images, as illustrated in Figure 4.1a. Subsequently, the size distribution is analyzed by fitting a log-normal distribution to the histogram (Fig. 4.1b) using OriginLab:

$$f(d) = \frac{1}{d\sqrt{2\pi\sigma^2}} \exp\left(-\frac{(\ln(d) - \mu)^2}{2\sigma^2}\right)$$

where d is the mean particle diameter, σ is the standard deviation, and μ the mean of the logarithmic values. The SEM image in figure 4.1a indicates that

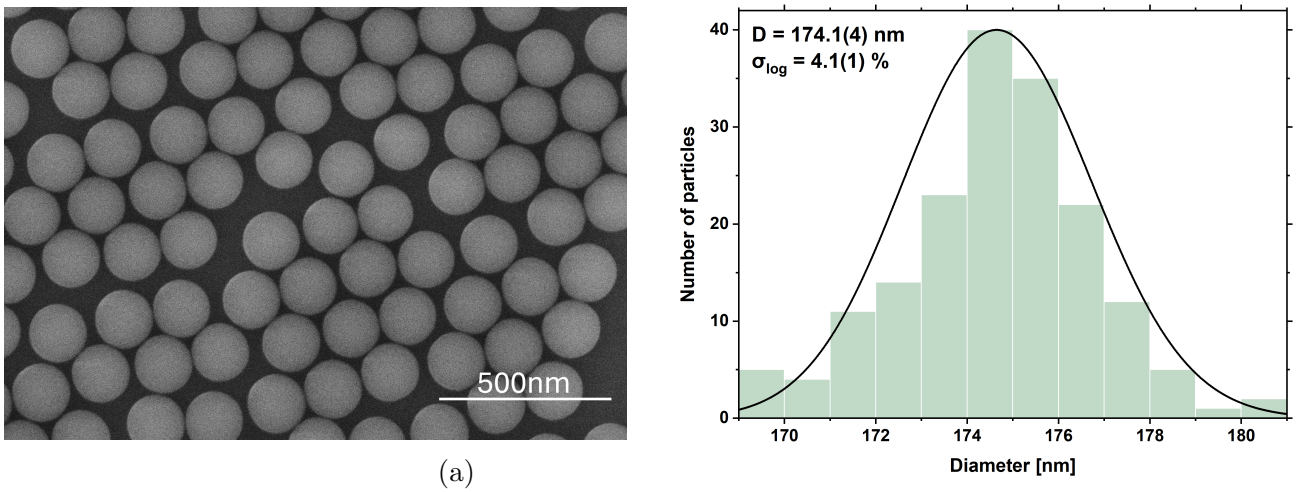

(a) (b)

Figure 4.1: a) SEM image of the sample containing 5μl of the NP dispersion. b) Histogram of the evaluated size distribution.

the NPs used in this thesis are of spherical shape with a mean diameter of 174.1(4) nm and a size distribution σ_{log} of 4.1(1)% as shown in figure 4.1b. This indicates a highly monodisperse NP distribution. SEM clearly revealed that the particles are regular spherical particles and once deposited over the silicon substrate, tend to self-organize into a regular hexagonal arrangement.

SAXS is measured to obtain ensemble-averaged information of the NP size and size distribution. While SEM is useful in obtaining a detailed visualization, SAXS averages the properties of a very large number of particles simultaneously. The SAXS measurement was conducted at the GALAXI instrument described in section 3.3 in the configuration explained in 3.3.1. The sample was measured at the long sample-to-detector distance LSDD = 3.53m. The silica nanoparticles dispersions were filled in quartz glass capillaries from Hilgenberg GmbH with an outside diameter of 1.5 mm and a wall thickness of 0.01 mm. The capillaries filled with the water as solvent and the nanoparticles dispersion, as well as an empty capillary, were measured under the same conditions as a reference sample for the subtraction of the background. The measurement time was approximately 1.5h per sample. Figure 4.2 shows the SAXS plot for a silica nanoparticles dispersion with a concentration of 0.011%. The data was analyzed with SasView [37] by assuming a spherical shape model. Fitting the spherical model to the experimental data leads to a particles radius of 87.7(5) nm and size distribution of σ_{log} 3.8(0)%,

which closely aligns with the parameters obtained from SEM. The parameters used to fit the SAXS data and the obtained size and size distribution are listed in table 4.1.
Table 4.2 displays the values obtained from SEM and SAXS. When comparing the data, the values closely align, confirming the average particle diameter of approximately 175 nm and a monodisperse size distribution of around 4%.

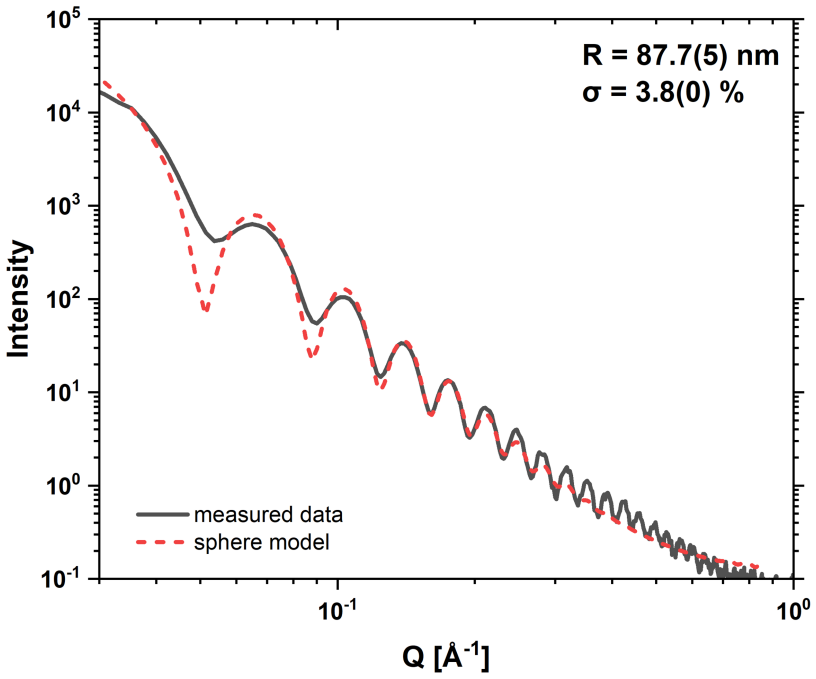

Figure 4.2: SAXS data of SiO_2 depicting the measured data (black line) and the sphere model (red line).

SAXS parameters				
Sample name	R[nm]	σ_{log}%	$SLD_{solvent}$ [10^{-6} Å^{-2}]	$SLD_{particle}$ [10^{-6} Å^{-2}]
SIO_2 - 0.011%	87.7(5)	3.8(0)	9.45	15.4

Table 4.1: SAXS parameters obtained from fitting the SAXS data with a spherical form factor shown in Fig. 4.2 using SasView. The table depicts the radius R of the sphere, the log-normal size distribution σ_{log}, and the $SLD_{solvent}$ and $SLD_{particle}$.

Comparison of SEM and SAXS		
Parameter	SEM	SAXS
R [nm]	87.7(5)	87.0(7)
d [nm]	174.1(4)	175.5(0)
σ_{log}%	4.1(1)	3.8(0)

Table 4.2: Comparison of the NP radius R, diameter d, and size distribution σ_{log} obtained from SEM and SAXS.

4.2 Formation of Nanosphere Monolayers and Local Characterization by SEM

An improved method of drop-casting is used in this thesis to form ordererd monolayers of SiO_2 established by Qdemat et al. (2020) [12]. In that work, the solution used for the formation of the monolayer consisted of 0.1 vol% stearyl-grafted silica nanoparticles and 0.1 vol% stearyl alcohol, with toluene serving as the solvent. Then, 5 μl of the dispersion was drop-casted with a micropipette onto silicon wafers, the same substrates that are used in this thesis. After drop-casting, the sample was kept stationary and its container was covered with a film to slow solvent evaporation rate. Additionally, the samples were annealed in a heat treatment step at 70 °C for 10 days to further enhance the quality of the monolayer.
Here, a solution consoist of 0.1 vol% of ungrafted 200 nm silica NP and 0.1 vol% stearyl alcohol and ethanol as solvent as described in section 3.1.2. The improved drop-casting method was applied to the larger 200 nm silica NP with the aim of conducting a drop volume series investigation to determine the optimum drop volume to obtain highly ordered self-assembled monolayers of ungrafted silica NPs of $\approx$ 200 nm in diameter over a large area on a Si substrate. Then, the samples were annealed at the same temperature and duration to study whether an additional heat treatment leads to additional improvement in the monolayer quality.
Figure 4.3 shows the drop volume series starting from 5 μl - 40 μl in 5 μl step sizes at the same magnification with a scale of 5 μm. The images demonstrate a clear correlation between drop volume and the amount of NP needed to cover the substrate. Smaller drop volumes result in monolayers that are not spread homogeneously over the substrate, as the NP amount is insufficient. This creates separated islands with ordered domains. Increasing the drop volume to 25 μl results in the best coverage, as evidenced by the highest long-range ordering observed among the different volumes. With further increases in drop volume, multilayers begin to form. However, drop volumes

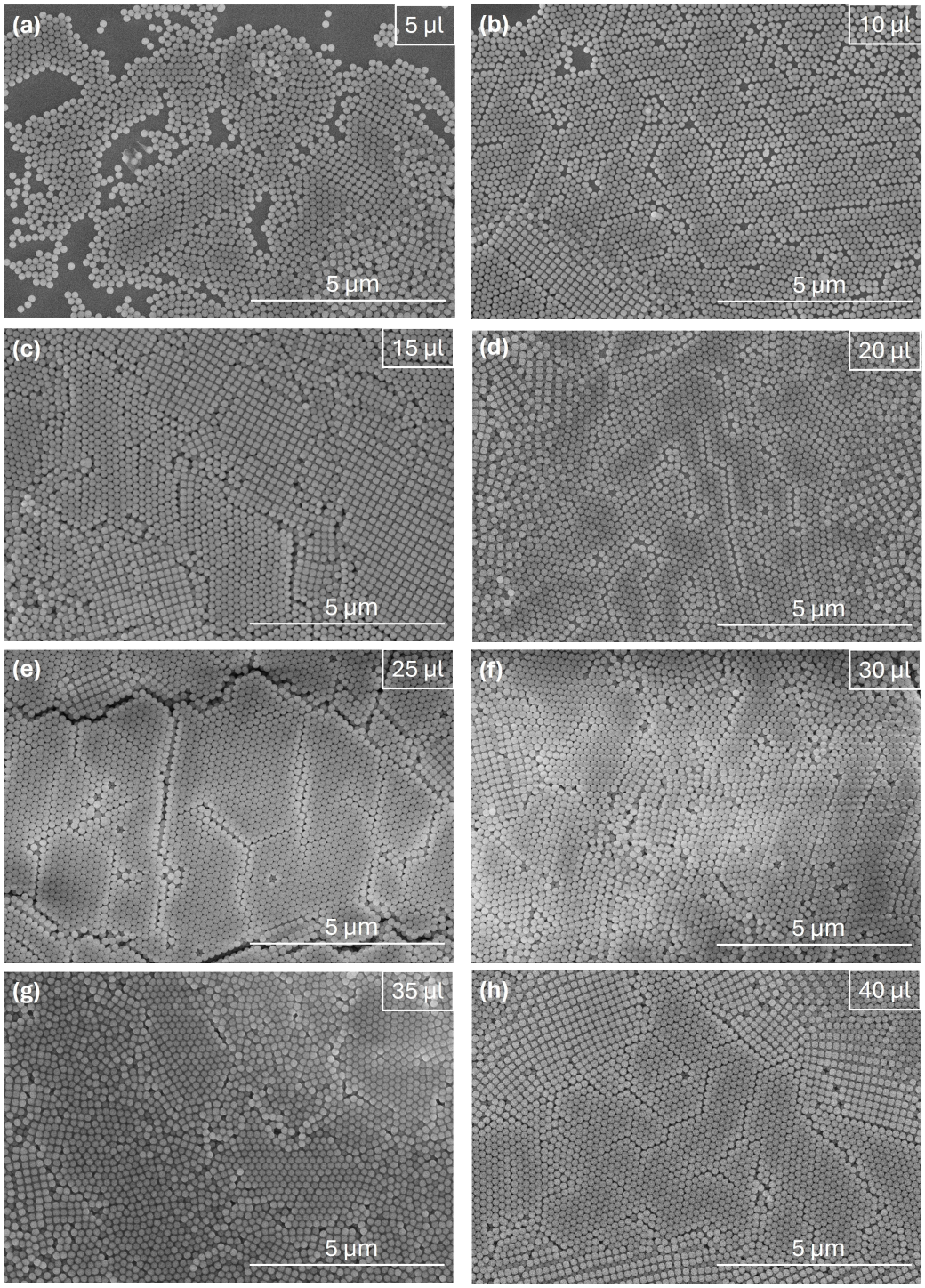

Figure 4.3: (a)-(h): SEM-images of the drop volume series from 5 μl - 40 μl before heat treatment.

above 25 μl appear to induce more unordered, random arrangements of the NPs. This may be attributed to the enhanced Marangoni flow observed in larger droplets, which can lead to more complex fluid dynamics. Furthermore, larger drop volumes can result in variations in particle interactions across the droplet, leading to an uneven NP distribution. This can manifest as areas with dense packing or sparse NP distribution.
Furthermore, not only hexagonal but also ordered square structures can be observed. Usually, spherical NPs tend to organise themselves into hexagonal close-packed structures due to isotropic interactions. However, interparticle forces described in section 2.1.2 might encourage a square arrangement through directional bonding or dipole interactions rather than isotropic packing.
To improve the NPs ordering and decreasing defects such as cracks and other defects, the samples were heat treated in an oven at 70 °C for 10 days. The reasoning behind it is melting the stearyl alcohol in the monolayers, since its melting point is at 59.5 °C and is solid at room temperatures. This could induce NPs to move freely again and enable them to self-assemble further into ordered structures. Then, in order to discontinue this self-assembly process, simply cooling the sample to room temperature solidifies the ordered layer with only a minor change in the volume. Figure 4.4 shows the SEM images of the drop volume series after heat treatment. As seen from SEM, an improvement in long-range order and a slight decrease of defects can generally be observed. Especially for the 25 μl sample, domains of ordered structures are correlated over larger distances, overall indicating it to be the optimum drop volume. This is illustrated by figure 4.5, where a fast Fourier transform (FFT) of the annealed 25 μl sample shows sharp peaks, which confirms a long-range order of NPs.

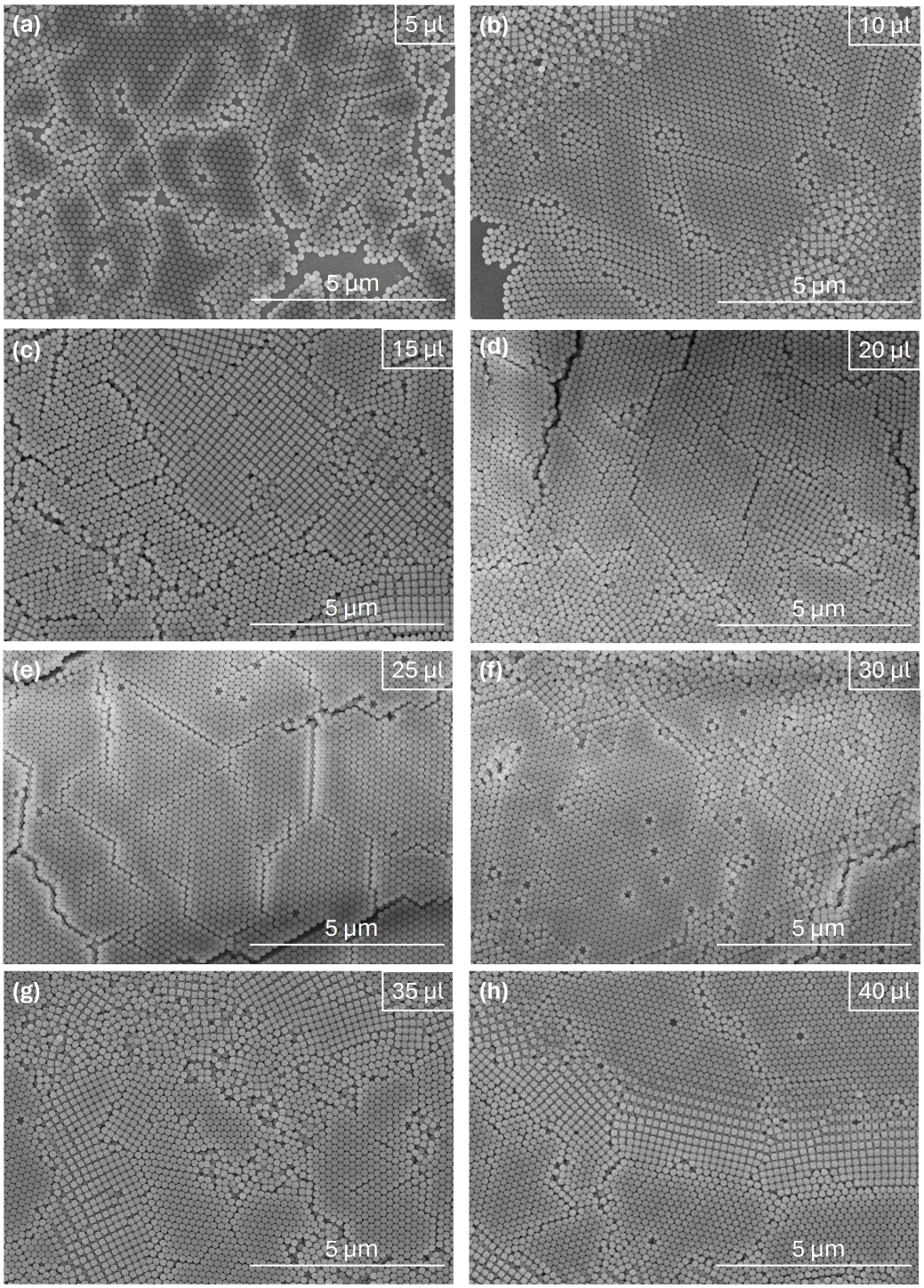

Figure 4.4: (a)-(h): SEM-images of the drop volume series from 5 μl - 40 μl, after heat treatment

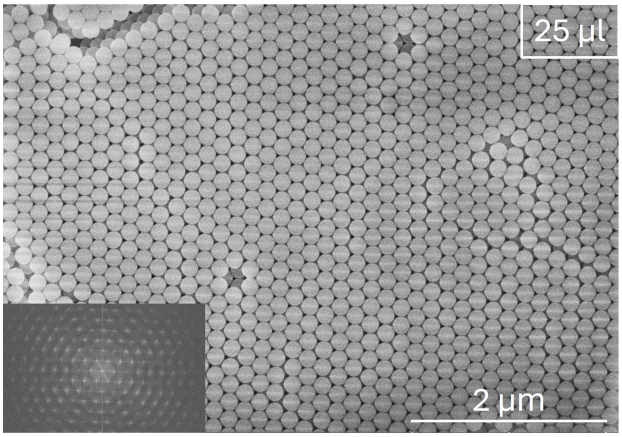

Figure 4.5: SEM image of the annealed 25 μl sample at a higher magnification, including its 2D Fourier transform pattern.

4.3 Global and Depth-Resolved Characterization by GISAXS and XRR

While SEM provides information of sample areas of a few microns, therefore GISAXS and XRR measurements were performed to provide global average structural information and confirm the findings of the previous section. GISAXS measurements were carried out at GALAXI (Sec. 3.3) and XRR measurements at Bruker D8 Advance (Sec. 3.4).

GISAXS measurements

The GISAXS measurements for all samples were measured before and after annealing at incident angles of $\alpha_i = 0.2°$ and at the longest sample-to-detector distance LSDD = 3.528m. The beam center and sample-to-detector distance are determined by a calibration measurement of silver behenate (AgBH). Figure 4.6 shows the 2-D GISAXS images in q-space of the entire drop volume series. Distinct vertical Bragg rods visible in all GISAXS patterns along the Q_y-direction which are especially noticeable for the 25 μl sample, implying a long-range periodic order of the NPs.

Diffuse rings are also observable for all GISAXS measurements, which which are related to the square of the Fourier transform of the particle shape (i.e., the form factor of the individual NPs) (Sec. 2.3.1). Furthermore, structure peaks at $Q_z = 1.25$ nm^{-1} appear and increase in intensity in relation to higher drop volumes The problem that the peak didn't appear with 15

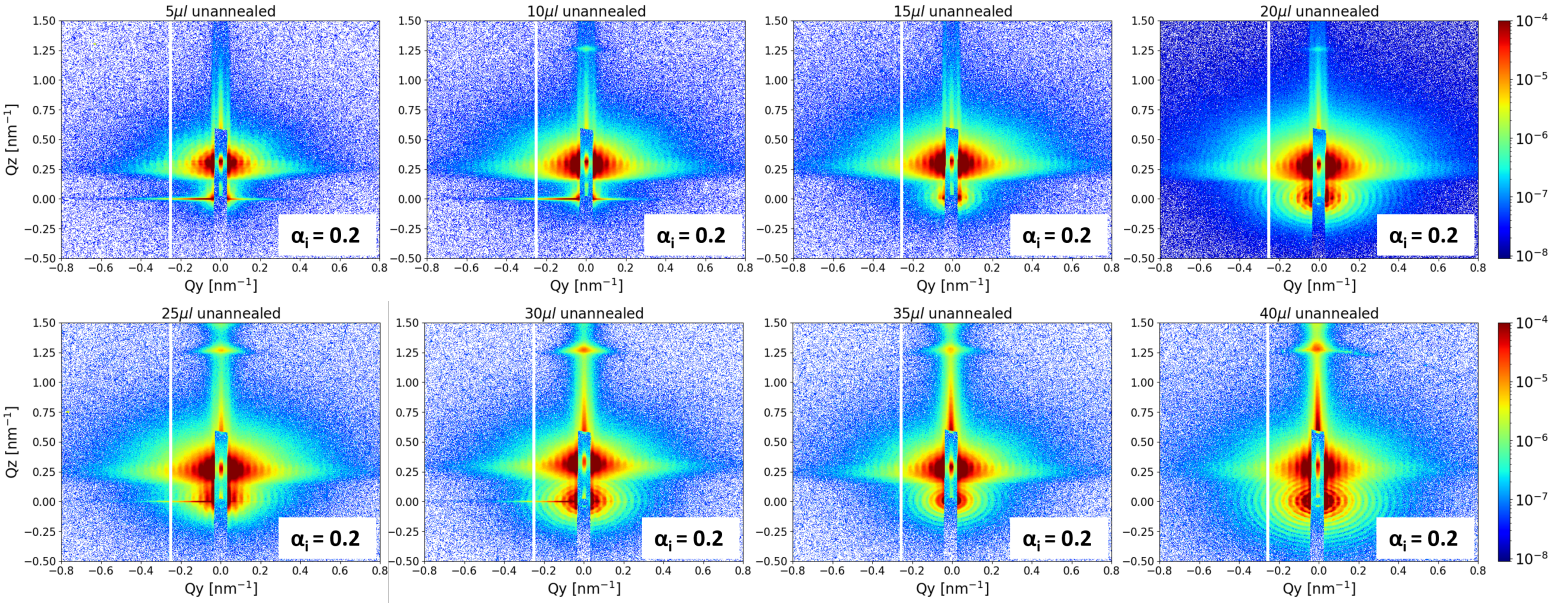

Figure 4.6: GISAXS measurements of the drop volume series before annealing. From left to right: Top row: 5 - 20 μl, bottom row: 25 - 40 μl.

Ml droplet??. These peaks seem to imply periodic structures at a real-space position of d $\approx$ 5 nm. While the exact nature of this structure peak remains uncertain, a potential explanation is that the ungrafted NPs in the dispersion undergo coating with a stearyl alcohol double layer. Following the drop-casting process, stearyl alcohol may form a periodic double layer between the substrate and NP monolayer, resulting in the observed structure peak along Q_z-direction.
To better compare the 2D GISAXS scattering patterns, an intensity integration around the specular peak along Q_y is perfomed of the entire drop volume series. Figure 4.7 depicts the intensity integration of the entire drop volume series as a function of intensity to Q_y.
From this it is clearly visible that the 25 μl sample contains the sharpest Bragg peak. It is indicative of more long-range correlated NP domains within the sample, as higher intensities stem from coherent interference after scattering which transpires only from ordered NP structures. The intensity peaks are spaced equally distant to each other, implying a NP monolayer ordering into square lattices.

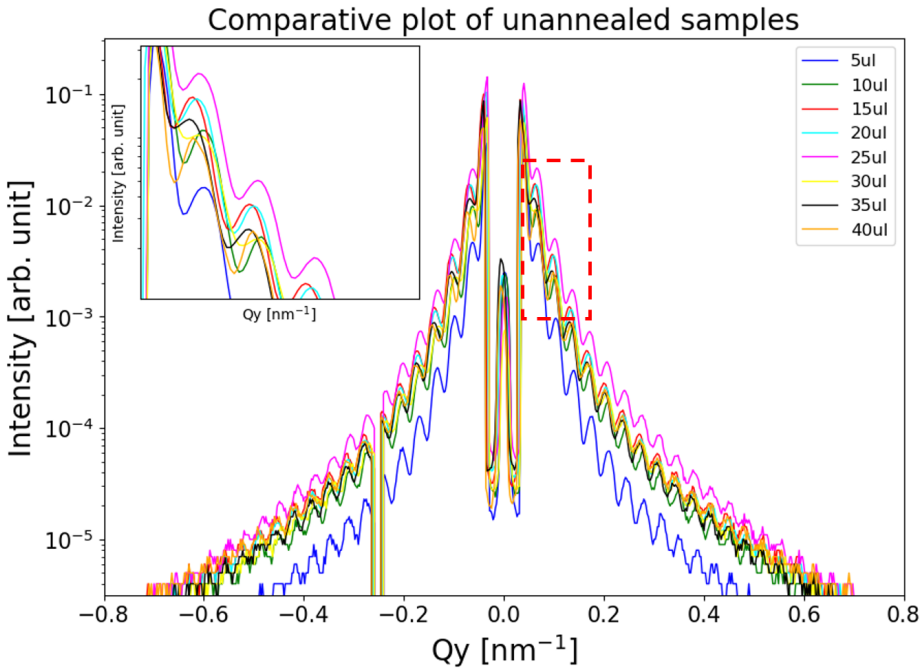

Figure 4.7: Comparative plot of the intensity integration for all samples before annealing.

Overall, the Bragg peaks become more intense and sharp after heat treating the samples for 10 days (Fig. 4.8). Again, the 25 μl sample shows an enhancement in Bragg rods along the Q_y-direction compared to other samples. In addition, these sharp peaks are also visible in the transmission part around the circular beam stop. As GISAXS provides structural information at a buried interface of 10 nm, Bragg peaks in the transmission part indicate an ordering of monolayers into multilayers. Furthermore, the structural peaks assumed to be stearyl alcohol layers at $Q_z = 1.25$ nm^{-1} have neatly completely vanished after heat treatment. This might be attributed to the melting of stearyl alcohol during annealing and the breakdown of a stearyl alcohol double layer. Figure 4.9 compares the intensity integration of the drop volume series after annealing. Again, the 25 μl sample shows the highest intensity peaks compared to the rest, which confirms the SEM findings from the previous section of this drop size being the most optimal volume. To determine whether heat treating the samples improves monolayer formation, comparative plots for all samples are depicted in figure 4.10. Generally, annealing leads to more ordered structures and long-range ordering, as indicated by the intensity increase of the Bragg peaks.

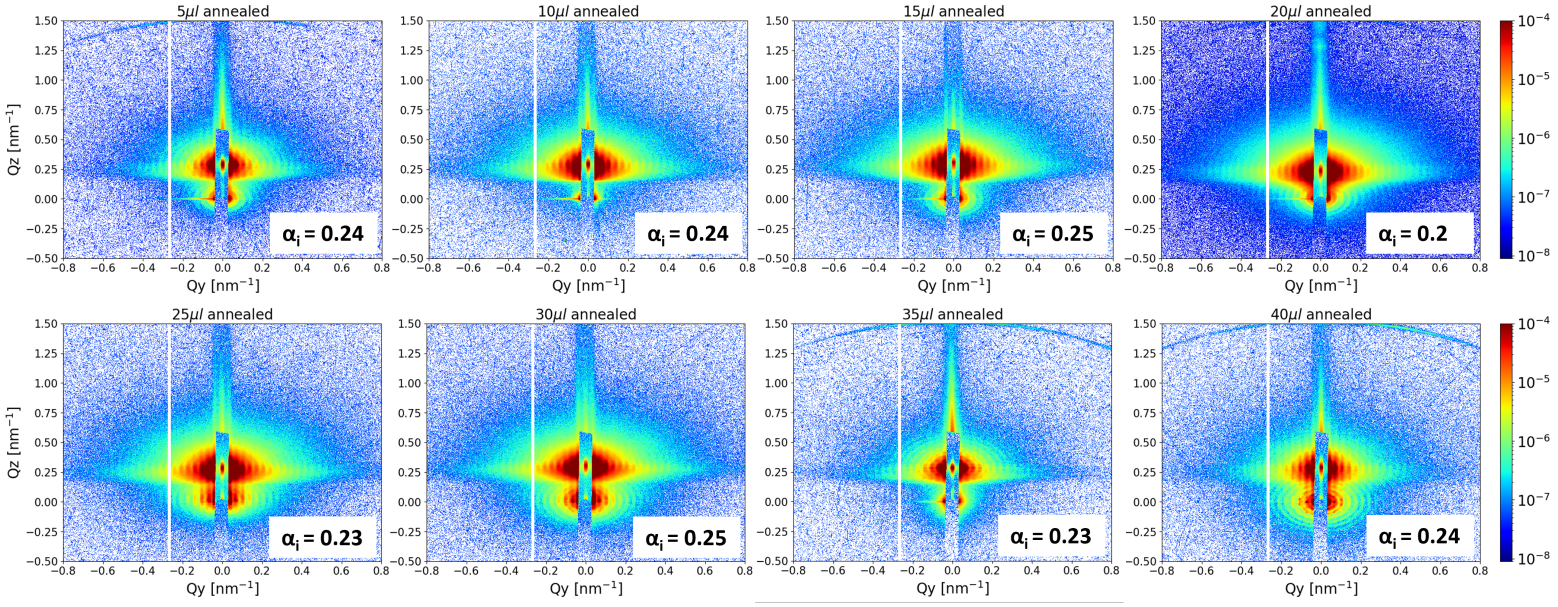

Figure 4.8: GISAXS measurements of the drop volume series after annealing. From left to right: Top row: 5 - 20 μl, bottom row: 25 - 40 μl.

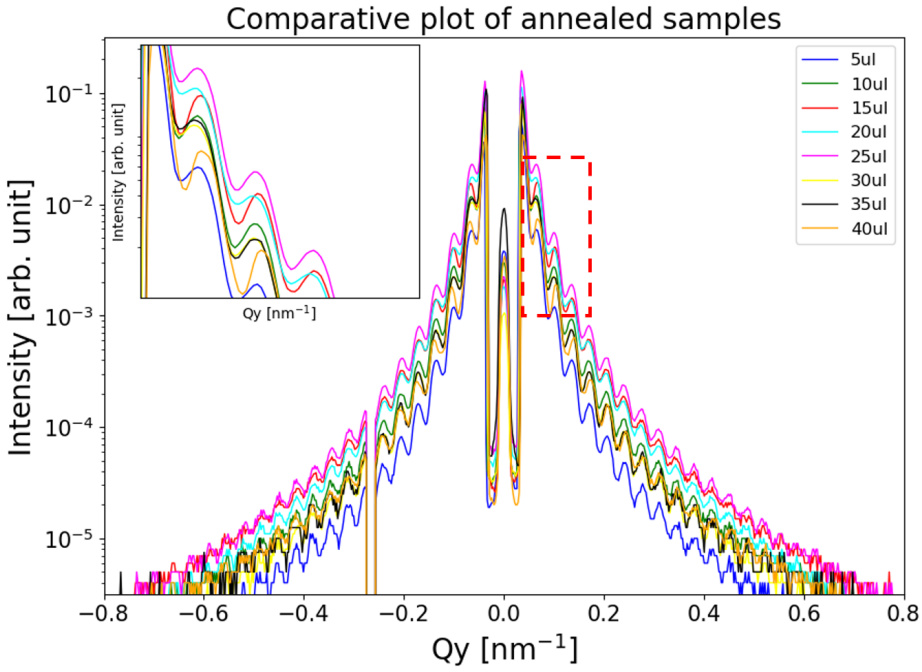

Figure 4.9: Comparative plot of the line integration for all samples after annealing.

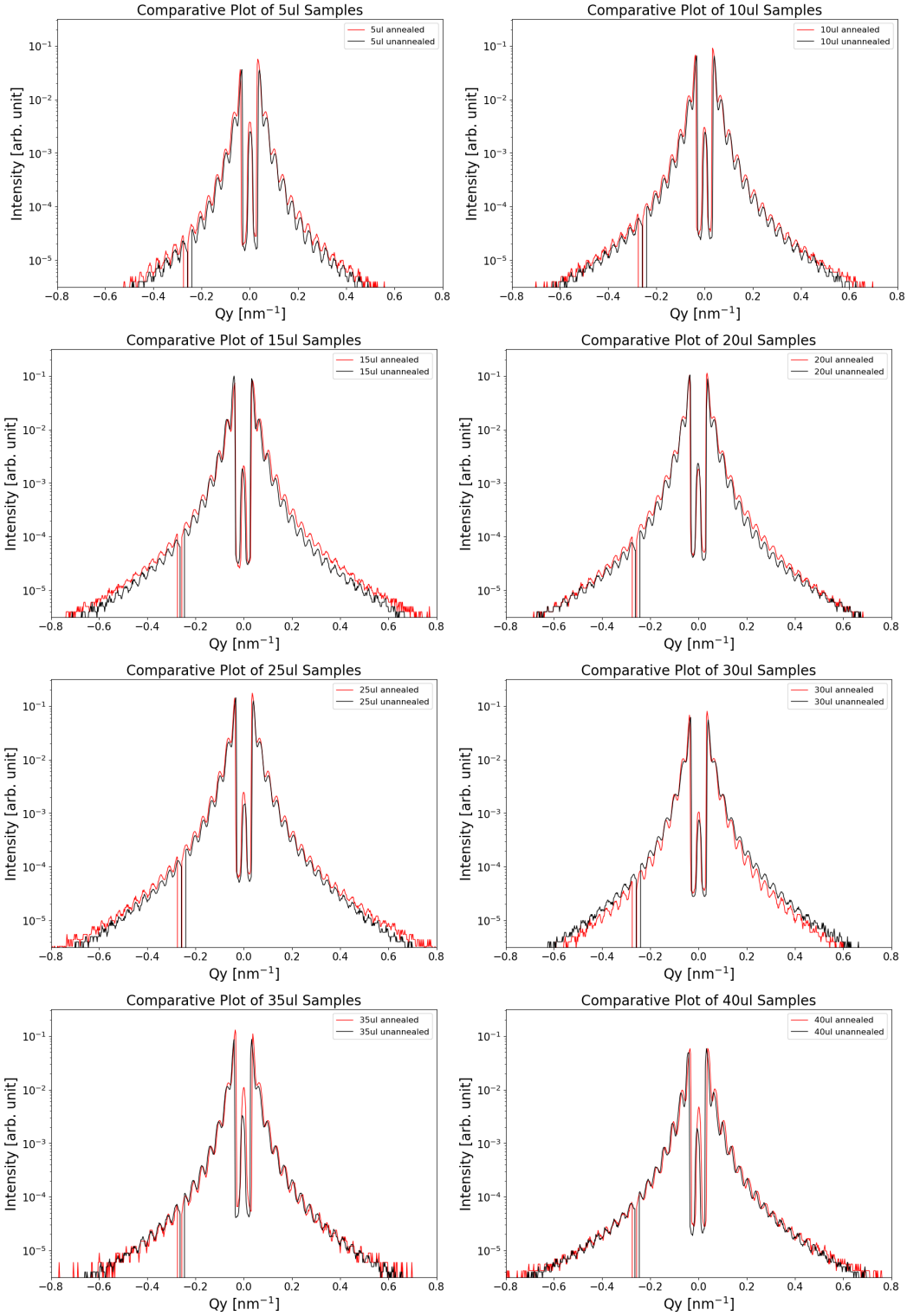

Figure 4.10: A comparison of each sample in the drop volume series before and after heat treatment. An overall trend in intensity increase and therefore ordered NP arrangement is observable.

XRR measurements

XRR measurements provide insight into the electron density distribution with respect to the vertical axis. In figure 4.11, it is visible that the critical angle α_c remains at the same position $Q_z = 0.32$ nm^{-1} and corresponds to the silicon substrate. When performing XRR measurements Kiessig fringes commmonly occur, which is not observable here. The reason for this is that the fringe spacing in Q_z depends on the film thickness. An increase in layer thickness leads to a decrease in fringe spacing and their amplitude. The reduction in amplitude is partly due to the increased path differences of the X-rays within the interface layer and the subsequent decrease in coherent interference. Due to the NPs forming monolayers with a layer thickness of around 200 nm, Kiessig fringes are not visible. However, a structure peak is evident at $Q_z = 1.26$ nm^{-1} for all samples before heat treatment. In addition, after heat treating this structure peak disappears. For both GISAXS and XRR, peaks at the same Q_z value can indicate structural features with similar periodic ordering perpendicular to the surface. However, the nature of these characteristics can be interpretated differently. For GISAXS peaks along Q_z, they usually refer to periodic arrangements such as the NP monolayers in this thesis, while XRR peaks often relate to multi-layer structures. A correlation between peaks in GISAXS and XRR as seen in figure 4.11 can suggest that the surface or burried interface features observed with GISAXS might influence the overall thickness profile measures by XRR.

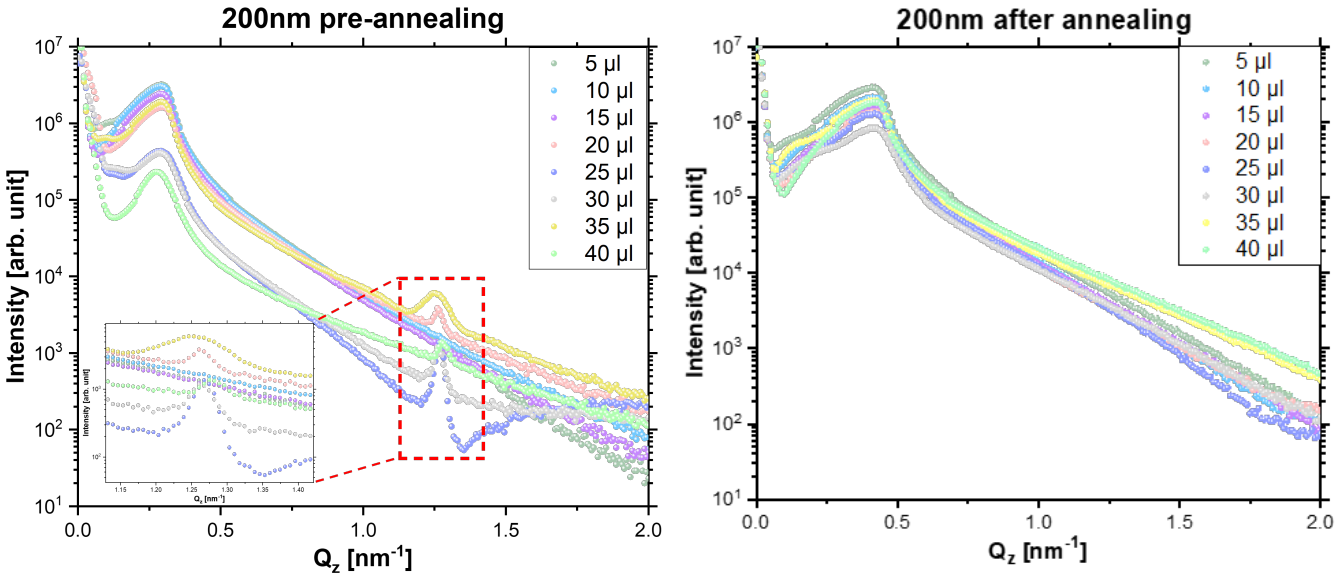

Figure 4.11: XRR measurement of the drop volume series before annealing and zooming into the structure peak at $Q_z = 1.26$ nm^{-1} (left) and after annealing (right).

Chapter 5

Summary and Outlook

In this thesis, the self-assembly of uncoated silica nanoparticles with a diameter of d $\approx$ 200 nm has been studied. The research used an improved drop-casting method on the basis of using stearyl alcohol as an assistant and a heat treatment step to improve monolayer formation. The size and size distribution of the nanoparticles has been evaluated using SEM and SAXS, resulting in a mean diameter of d = 174 nm and a size distribution of aroung 4%. Key to the study was finding the optimal drop volume to obtain highly ordered arrangments of ungrafted silica NPs of $\approx$ 200 nm in diameter over a large area on a Si substrate, which was found to be 25 μl through a drop volume series investigation. The characterization of these samples were carried out through SEM, XRR, and GSIAXS. These methods provided insight into the ordering between NPs both before and after sample annealing. The monolayers showed improvement in quality after determining the right drop volume and after annealing, however several defects such as cracks, missing particles and uneven particle distribution are still visible. To further improve monolayer quality, increasing annealing time and temperature might lead to more ordered structures since larger particles may self-assemble and move slower due to their size. In addition to that, grafting the nanoparticles with a stearyl alcohol layer can improve self-assembly by decreasing agglomeration and balance particle distribution on the substrate.

References

[1] G.M. Whitesides and M. Boncheva. "Beyond molecules: Self-assembly of mesoscopic and macroscopic components". In: *Proceedings of the National Academy of Sciences* 99.8 (2002), pp. 4769–4774. DOI: 10.1073/pnas.082065899.

[2] Y. Xia et al. "Monodispersed Colloidal Spheres: Old Materials with New Applications". In: *Advanced Materials* 12.10 (2000), pp. 693–713. DOI: 10.1002/(SICI)1521-4095(200005)12:10<693::AID-ADMA693>3.0.CO;2-J.

[3] A. Yamamura et al. "Wafer-scale, layer-controlled organic single crystals for high-speed circuit operation". In: *Science Advances* 4.2 (2018), eaao5758. DOI: 10.1126/sciadv.aao5758.

[4] K. Ariga et al. "Self-assembly as a key player for materials nanoarchitectonics". In: *Science and Technology of Advanced Materials* 20.1 (2019), pp. 51–95. DOI: 10.1080/14686996.2018.1553108.

[5] J. Liu et al. "Sintering-Resistant Nanoparticles in Wide-Mouthed Compartments for Sustained Catalytic Performance". In: *Scientific Reports* (2017). DOI: 10.1038/srep41773.

[6] N. Abid et al. "Synthesis of nanomaterials using various top-down and bottom-up approaches, influencing factors, advantages, and disadvantages: A review". In: *Advances in Colloid and Interface Science* 300 (2022), p. 102597. DOI: 10.1016/j.cis.2021.102597.

[7] V. Lotito and T. Zambelli. "Approaches to self-assembly of colloidal monolayers: A guide for nanotechnologists". In: *Advances in Colloid and Interface Science* 246 (2017), pp. 217–274. DOI: 10.1016/j.cis.2017.04.003.

[8] S. Su et al. "Annealing-Assisted Dip-Coating Synthesis of Ultrafine Fe3O4 Nanoparticles/Graphene on Carbon Cloth for Flexible Quasi-Solid-State Symmetric Supercapacitors". In: *ACS Applied Energy Materials* 3.9 (2020), pp. 9379–9389. DOI: 10.1021/acsaem.0c01745.

[9] P.G. Born. "Role of Meniscus Shape in Large-Area Convective Particle Assembly". In: *Crystallization of Nanoscaled Colloids*. Heidelberg: Springer International Publishing, 2013, pp. 23–50. DOI: 10.1007/978-3-319-00230-9_2.

[10] Z. Chen et al. "A floating-gate field-effect transistor memory device based on organic crystals with a built-in tunneling dielectric by a one-step growth strategy". In: *Nanoscale* 16 (7 2024), pp. 3721–3728. DOI: 10.1039/D3NR06278C.

[11] A. A. Barzinjy et al. "Biosynthesis and characterisation of zinc oxide nanoparticles from Punica granatum (pomegranate) juice extract and its application in thin films preparation by spin-coating method". In: *Micro & Nano Letters* 15.6 (2020), pp. 415–420. DOI: 10.1049/mnl.2019.0501.

[12] A. Qdemat et al. "Self assembled monolayer of silica nanoparticles with improved order by drop casting". In: *RSC Adv.* 10 (31 2020), pp. 18339–18347. DOI: 10.1039/D0RA00936A.

[13] D. Luo, C. Yan, and T. Wang. "Interparticle Forces Underlying Nanoparticle Self-Assemblies". In: *Small* 11.45 (2015), pp. 5984–6008. DOI: 10.1002/smll.201501783.

[14] J. Masliyah and S. Bhattacharjee. *Electrokinetic and Colloid Transport Phenomena*. 2006, pp. 398–400. ISBN: 9780471788829. DOI: 10.1002/0471799742.

[15] H. Kamiya et al. "Chapter 3 - Characteristics and Behavior of Nanoparticles and its Diapersion Systems". In: *Nanoparticle Technology Handbook*. Ed. by M. Hosokawa et al. Amsterdam: Elsevier, 2008, pp. 113–176. ISBN: 978-0-444-53122-3. DOI: 10.1016/B978-044453122-3.50006-4.

[16] Y. Min et al. "The role of interparticle and external forces in nanoparticle assembly". In: *Nature Materials* 7 (2008), pp. 527–538. DOI: 10.1038/nmat2206.

[17] B. Xu et al. "Multifunctional mesoporous silica nanoparticles for biomedical applications". In: *Signal Transduction and Targeted Therapy* 8 (2023). DOI: 10.1038/s41392-023-01654-7.

[18] J. Peerzada et al. "Multifaceted Application of Silica Nanoparticles. A Review". In: *Silicon* 12 (2020). DOI: 10.1007/s12633-019-00229-y.

[19] H.B. Bohidar and K. Rawat. *Design of nanostructures : self-assembly of nanomaterials*. Wiley VCH, 2017, pp. 188 –193. ISBN: 978-3-527-81041-3.

[20] C.C.M.C. Carcouët et al. "Nucleation and Growth of Monodisperse Silica Nanoparticles". In: *Nano Letters* 14.3 (2014), pp. 1433–1438. DOI: 10.1021/nl404550d.

[21] V. Selvarajan, S. Obuobi, and P. Ee. "Silica Nanoparticles—A Versatile Tool for the Treatment of Bacterial Infections". In: *Frontiers in Chemistry* 8 (2020), p. 602. DOI: 10.3389/fchem.2020.00602.

[22] I. W. Hamley. *Small-angle scattering: theory, instrumentation, data and applications*. Chichester, UK: John Wiley and Sons, 2021. ISBN: 9781119768302.

[23] T. Li, A.J. Senesi, and B. Lee. "Small Angle X-ray Scattering for Nanoparticle Research". In: *Chemical Reviews* 116.18 (2016), pp. 11128–11180. DOI: 10.1021/acs.chemrev.5b00690.

[24] G. Renaud, R. Lazzari, and F. Leroy. "Probing surface and interface morphology with Grazing Incidence Small Angle X-Ray Scattering". In: *Surface Science Reports* 64.8 (2009), pp. 255–380. ISSN: 0167-5729. DOI: 10.1016/j.surfrep.2009.07.002.

[25] A. Gibaud, M. S. Chebil, and T. Beuvier. "X-Ray Reflectivity". In: *Surface Science Techniques*. Ed. by G. Bracco and B. Holst. Berlin, Heidelberg: Springer Berlin Heidelberg, 2013, pp. 191–216. ISBN: 978-3-642-34243-1. DOI: 10.1007/978-3-642-34243-1_7.

[26] F.J. Arriagada and K. Osseo-Asare. "Phase and dispersion stability effects in the synthesis of silica nanoparticles in a non-ionic reverse microemulsion". In: *Colloids and Surfaces* 69.2 (1992), pp. 105–115. DOI: 10.1016/0166-6622(92)80221-M.

[27] F.J. Arriagada and K. Osseo-Asare. "Synthesis of Nanosize Silica in a Nonionic Water-in-Oil Microemulsion: Effects of the Water/Surfactant Molar Ratio and Ammonia Concentration". In: *Journal of Colloid and Interface Science* 211.2 (1999), pp. 210–220. DOI: 10.1006/jcis.1998.5985.

[28] K. Osseo-Asare and F.J. Arriagada. "Preparation of SiO2 nanoparticles in a non-ionic reverse micellar system". In: *Colloids and Surfaces* 50 (1990), pp. 321–339. DOI: 10.1016/0166-6622(90)80273-7.

[29] D.R. Lide and G.W.A. Milne. "Handbook of data on organic compounds". In: CRC Press, 1994, p. 3687.

[30] W. Zhou et al. "Fundamentals of Scanning Electron Microscopy (SEM)". In: *Scanning Microscopy for Nanotechnology: Techniques and Applications*. New York, NY: Springer New York, 2007, pp. 1–40. DOI: 10.1007/978-0-387-39620-0_1.

[31] A. Qdemat. "Nanoparticle assemblies: Order by self-organization and collective magnetism". PhD thesis. RWTH Aachen University, 2020.

[32] E. Kentzinger, M. Kruteva, and U. Rücker. "GALAXI: Gallium anode low-angle x-ray instrument". In: *Journal of large-scale research facilities JLSRF* 2 (2016). DOI: 10.17815/jlsrf-2-109.

[33] G. Pospelov et al. "*BornAgain*: software for simulating and fitting grazing-incidence small-angle scattering". In: *Journal of Applied Crystallography* 53.1 (2020), pp. 262–276. DOI: 10.1107/S1600576719016789.

[34] Nejati, A., Svechnikov, M., and Wuttke, J. "BornAgain, software for GISAS and reflectometry: Releases 1.17 to 20". In: *EPJ Web Conf.* 286 (2023), p. 06004. DOI: 10.1051/epjconf/202328606004.

[35] A. Glavic. "Multiferroicity in oxide thin films and heterostructures". PhD thesis. RWTH Aachen University, 2012.

[36] C. Schneider, W. Rasband, and K. Eliceiri. "NIH Image to ImageJ: 25 years of image analysis". In: *Nature Methods* 9 (2012). DOI: 10.1038/nmeth.2089.

[37] M. Doucet et al. *SasView version 5.0.4*. 2021. DOI: 10.5281/zenodo.4467703.